Infinitely Many Optimal Iso-Impulse Trajectories in Two-Body Dynamics

by

Keziban Saloglu

A thesis submitted to the Graduate Faculty of
Auburn University
in partial fulfillment of the
requirements for the Degree of
Master of Science

Auburn, Alabama
August 5, 2023

Keywords: impulsive trajectory, trajectory optimization, optimal control, maneuver placement, primer vector theory

Approved by

Ehsan Taheri, Chair, Assistant Professor of Aerospace Engineering
Damon Landau, Mission Formulation Engineer of California Institute of Technology
Davide Guzzetti, Assistant Professor of Aerospace Engineering
Nan Li, Assistant Professor of Aerospace Engineering

Abstract

Rendezvous maneuvers are designed to match the position and velocity vectors of a target body (e.g., planet, comet, satellite) whereas transfer maneuvers are designed to match the orbital elements of the target body, except for the true anomaly under a two-body dynamical model. The question of how many impulsive maneuvers are necessary to minimize the total delta-v, Δv, for a transfer-type maneuver, has remained open for decades. In addition, efficient maneuver placement is an important step to generate impulsive trajectories. Recently, the introduction of optimal switching surfaces revealed the existence of iso-impulse trajectories with different numbers of impulses for fixed-time rendezvous maneuvers. The multiplicity of minimum-Δv impulsive trajectories for long-time-horizon maneuvers is studied in this work. One notable feature of these extremal impulsive trajectories is that many of the impulses are applied at a specific position, highlighting the significance of what we coin as "impulse anchor positions." The impulse anchor position is chosen to break up the total impulse into multiple impulsive maneuvers while respecting the primer vector theory. It is demonstrated that under the inverse-square gravity model, multiple-impulse, minimum-Δv solutions can be generated using a fundamental two-impulse solution, which provides the impulse anchor positions as well as the impulse direction and magnitude. Leveraging the two-impulse base impulsive solution, an analytic method is developed to generate multiple-impulse minimum-Δv trajectories by forming algebraic $\Delta v-$ allocation problems.

In addition to recovering all impulsive solutions for a multi-revolution benchmark problem from the Earth to asteroid Dionysus, the minimum-Δv solutions are classified and it is shown that there are infinitely many optimal iso-Δv solutions (i.e., requiring the same total Δv). The proposed method allows providing analytic bounds on the lower (required) and upper (allowable) number of impulses for three important classes of maneuvers: fixed-terminal-time rendezvous, free-terminal-time rendezvous, and phase-free transfer. A new interpretation of the primer vector for impulsive extremals with phasing orbits is proposed.

Acknowledgments

I would like to extend my gratitude to my family who have shown endless support even from a 9751 km distance between us. Graduate school has been a challenging journey, and I am fortunate to have their support and encouragement. Without you, I wouldn't be where I am today.

I am truly thankful to all my friends (they know themselves, even if I don't mention their names here) around the world, my ACELab fellows, Davis 153 office mates. Their companionship, support, and friendship have been invaluable. Thank you for understanding me, listening to me, and helping me whenever I needed a helping hand.

I would like to thank my advisor, Dr. Ehsan Taheri. His support and guidance have been instrumental over the past two years. He has encouraged me to reach beyond my limits, enabling me to achieve significant learning outcomes and gain invaluable research experience in trajectory optimization and optimal control.

I am also thankful to my outstanding committee members, Dr. Damon Landau, Dr. Davide Guzzetti, and Dr. Nan Li. I deeply appreciate your time and efforts in reading and providing your invaluable feedback for this study. Additionally, I am thankful to Dr. Landau for his insightful ideas and constructive feedback during the process of writing a journal paper, which is one of the outcomes of my MS.c. thesis.

Lastly, I would like to thank Auburn University, Samuel Ginn College of Engineering, and the Department of Aerospace Engineering for their financial support through the Presidential Fellowship that has partially supported my studies.

Table of Contents

List of Figures

List of Tables

Chapter 1

Introduction

Exploration of space is one of the ongoing goals of mankind. Exploring the universe around our planet, and even exploring our planet, is enabled by space exploration. Starting from Kepler, defining laws of planetary motion, and continuing with Newton deriving inverse-square law and gravitational force relations, we first wanted to understand the motion of the celestial bodies. Fast forward to technological advancements, the first spacecraft was launched into Earth's orbit. Later advancements include accomplishing the first human steps on the Moon. Since then, more and more spacecraft have been designed and built to serve: scientific missions, telecommunication, reconnaissance, and permanent establishment beyond the low Earth orbits. To accomplish all of these challenging tasks, the spacecraft has to travel an optimal trajectory (with respect to an optimality objective/goal) as well as use the limited resources on board efficiently. Therefore, it is crucial to generate optimal trajectories for successful missions, which leads to the typical classes of minimum-time and minimum-fuel problems for spacecraft trajectory optimization. These problems are challenging since the dynamics are nonlinear, there exist discontinuities in the state and control variables, there are disturbing forces acting on the spacecraft, and the number of required maneuvers is not usually known *a priori* [1].

1.1 Motivation

Impulsive trajectory optimization remains one of the fundamental tasks in designing space missions. Optimal impulsive trajectories minimize the total Δv (delta-v) needed to perform a mission. The total Δv can be defined as the sum of all velocity changes due to the acceleration

exerted on the spacecraft by its propulsion system. The total Δv can be related to the propellant consumption through the Tsiolkovsky rocket equation.

An important aspect of impulsive trajectories is the optimal placement of the impulsive maneuvers along the trajectory, as well as the total number of impulses needed to perform minimum-Δv maneuvers. Among those who studied space flights, Theodore Edelbaum's research on trajectory optimization began in 1954, and he became one of the pioneering contributors to the rapidly growing field of space trajectory optimization. In 1967, he wrote an influential paper titled "How many impulses?" with a survey on the number of impulses required for different minimum-Δv impulsive trajectories [2]. This is a fundamental and challenging question in astrodynamics and has been rigorously studied by some of the greatest intellectuals in astrodynamics/trajectory optimization for decades [3].

In a recent study, Taheri and Junkins introduced the idea of the *optimal switching surfaces* using a continuation-based method [4]. The switching surface notion establishes an intuitive, but rigorous connection between (continuous) low-thrust and impulsive trajectories. The switching surface is obtained by solving a minimum-fuel low-thrust trajectory optimization problem and applying a natural parameter continuation on the maximum acceleration or maximum thrust parameter. Increasing the acceleration gradually guides the solution closer to an impulsive solution. Optimal switching surface information provides an initial guess for the placement of the impulses. Taheri and Junkins also investigated the "How many impulses?" question and concluded that, in general, there is no unique answer to this question when total Δv is used as the only criterion under the inverse-square gravity model. In addition, they have shown that for the fixed-time rendezvous trajectories, there exist solutions with different numbers of impulses but the total value of Δv is identical (up to seven digits) on a few extremal multiple-impulse solutions for a benchmark problem from the Earth to asteroid Dionysus.

While Taheri and Junkins have answered Edelbaum's question within the context of fixed-time rendezvous maneuvers, the necessary number of impulses required for a transfer-type maneuver has remained open for decades. In this thesis, the solutions that have equal Δv values are defined as iso-impulse or iso-Δv solutions.

After consideration of the iso-impulse solutions, it is important to address the common features of these iso-impulse, long-time-horizon, and minimum-Δv trajectories. The work is extended to answer the question of "How many impulses?" for orbit-to-orbit transfer-type maneuvers or simply transfer maneuvers, as well as determining what are the upper and lower bounds on the number of impulses required for an impulsive transfer.

1.2 Objectives

This investigation aims to contribute to the generation of impulsive trajectories with a long-time horizon in the setting of a benchmark Earth to asteroid Dionysus (Earth-Dionysus) transfer- or rendezvous-type maneuvers. The method is motivated by the Earth-Dionysus problem. However, results can be expanded to different transfer problems. The generalization of the developed method is also demonstrated by solving two planet-centric impulsive trajectory optimization problems. Solving the Earth-Dionysus problem better demonstrates the utility of the method, since the Earth-Dionysus problem has a long time of flight. The common features among the iso-impulse solutions of the Earth-Dionysus problem are investigated to understand how these solutions can be generated without going through the steps of any continuation-based methods. The lower (required) and upper (possible) bounds on the number of impulses for the class of long-time horizon minimum-Δv trajectory optimization problems are given.

The goals are addressed by answering the following three questions:

1. *How these iso-impulse solutions can be generated for long-time-horizon multiple-revolution impulsive trajectories?*

   As will be shown herein, the existence of multiple phasing orbits is leveraged to recover the known impulsive solutions as well as the infinitely many solutions. An analytical method is proposed to generate infinitely many solutions starting from a base two-impulse solution. Obviously, solving a set of algebraic equations is computationally more efficient (by orders of magnitude) compared to existing methods that solve two-point boundary-value problems (TPBVPs) to generate the continuation-based initial

guess for the formulated direct-based Nonlinear Programming (NLP) problem. Therefore, this method removes the step to go through solving multiple TPBVPs and solving an NLP problem. The problem of generating iso-impulse solutions reduces to solving a family of analytic Δv-allocation problems.

2. *How can we classify iso-impulse solutions? and what is the solution space for these families of solutions?*

   Impulsive trajectories are classified based on the number of revolutions a spacecraft makes on a) the initial orbit, b) on a finite, yet unknown number of phasing orbits, c) a phase-free two-impulse arc, and d) the target orbit. The solution envelopes (with respect to the orbital periods) are also presented to identify the solution space for a family of solutions.

3. *Can the infinitely many solutions be used to determine the upper and lower number of impulses for long-time-horizon multiple-revolution trajectories?*

   The analytic bounds on the lower and upper number of impulses are presented using an important feasibility relation (corresponding to the available time for performing phasing maneuvers). The classes of maneuvers that are characterized by the proposed method are extended to a) fixed-terminal-time rendezvous maneuvers, b) free-terminal-time rendezvous maneuvers, and c) free-terminal-time transfer maneuvers.

In this thesis, first, the benchmark Earth-Dionysus problem is considered. However, the results are applicable to general long-time-horizon, many-revolution impulsive trajectories. In order to show the utility of the method, two planet-centric problems are solved.

1.3 Previous Contributions

Previous contributions to the topics studied in this research effort are reviewed in this chapter.

1.3.1 Primer Vector Theory

One approach to finding optimal impulsive trajectories is to use Lawden's primer vector theory [5]. The primer vector theory provides the necessary conditions for optimality. The necessary conditions are defined in terms of the magnitude of the primer vector (i.e., the costate associated with the velocity vector, $\boldsymbol{p} = -\boldsymbol{\lambda}_v$, where $\boldsymbol{p}$ is the primer vector and $\boldsymbol{\lambda}_v$ is the costate associated with the velocity vector). Note that the negative coefficient is because the minimum principle is used.

Due to the importance of Lawden's impulsive necessary conditions, they are repeated here:

1. the primer vector and its first derivative are continuous everywhere,

2. the magnitude of the primer vector remains less than unity, i.e., $p = \|\boldsymbol{p}\| < 1$ except for the impulse times when $\|\boldsymbol{p}\| = 1$,

3. at the impulse time instance, the primer vector is a unit vector along the optimal direction of impulse, and

4. at any intermediate impulse time, $dp/dt = \dot{p} = \dot{\boldsymbol{p}}^\top \boldsymbol{p} = 0$.

The violation of necessary conditions provides several ways to obtain an improved impulsive solution, through adding mid-course impulses, adjusting impulse locations or times, and addition of terminal coast arcs [6, 7].

For linearized dynamics [8, 9], the set of necessary conditions become sufficient conditions and it is proven that the number of impulses is, at most, equal to the number of specified/fixed states at the final orbit [10]. The primer vector theory is also used for verifying the local optimality of the obtained impulsive solutions and it provides the optimal direction for the impulses. Linearized dynamics are mostly used for close-proximity problems that consider the rendezvous of two spacecraft. These rendezvous impulsive trajectories are considered for debris-removal, in-orbit operations, and docking maneuvers [11, 12, 13, 14, 15]

1.3.2 Impulsive Trajectory Optimization

Prior to the development of electric thrusters, spacecraft trajectories included only impulsive maneuvers, since the spacecraft are equipped with chemical rockets. Chemical rockets produce a large amount of thrust during a relatively short time interval of operation. This leads to continuous change in the velocity of the spacecraft, which is ideally modeled as an instantaneous velocity change, introducing a discontinuity to the velocity along the trajectories. Under a two-body dynamical model and in-between consecutive impulses, the motion of the spacecraft is governed by the (restricted) two-body dynamics. Then, the design variables for the impulsive trajectories are the location, time, direction, and magnitude of the impulse.

Early work on the impulsive trajectories is focused on the transfer, rendezvous, and intercept trajectories [16]. Impulsive trajectories can also offer reachability insights to show the reachability of the spacecraft with different constraints on the direction and the magnitude of the impulse [17, 18, 19]. Another constraint defining impulsive trajectories is having free-time and fixed-time trajectories. Oftentimes, the analytical approaches are used for preliminary analysis purposes. Analytical investigations of impulsive trajectories play an important role in classifying solutions. One notable analytical method is the Hohmann transfer [20]. Hohmann transfer can be used for analyzing transfers between circular coplanar orbits. It is proved that the optimal two-impulse transfer is cotangential to the circles at the periapsis and apoapsis of the connecting elliptical orbit. Also, it is shown that the Hohmann transfer is the global optimal solution [21] for a certain range of ratios of the radii of the final and initial orbits. Hohmann transfer can also be used for analyzing transfer maneuvers between coaxial, coplanar elliptical orbits. In order to improve two-impulse solutions for circular to circular planar transfers, the bi-elliptic transfer is introduced [22, 23]. Some of the studies considering specific geometrical orbit shapes and a constrained number of impulses are given in References [24, 25, 26, 27, 28, 29]. The survey paper of Gobetz and Doll includes the early studies, until 1969 [16].

As mentioned earlier, efficient maneuver placement for impulsive trajectories can also be achieved using the primer vector information. When a two-impulse solution is obtained for a trajectory, the time history of the primer vector magnitude provides information on the impulse

time and place to improve the solution. In doing so, a feasible sub-optimal impulsive solution can be improved to a local extremal solution that satisfied Lawden's optimality conditions. Typically, a hybrid solution approach is considered for such cases. The design variables are chosen as the impulse times and positions and the continuation of the trajectory is accomplished by solving Lambert's problem in the inner level of a Nonlinear Programming (NLP) solver. Therefore, these approaches are called hybrid methods, as they combine indirect-based primer vectors with direct solvers. Primer vector theory has been applied to many different types of impulsive trajectory optimization problems. For instance, optimization based on the primer vector theory is considered for coplanar and noncoplanar, circle-to-circle, and low-eccentricity fixed-time rendezvous problems for determining placement and the number of maneuvers [7, 30, 25, 31, 32, 33]. In these approaches, an initial feasible solution is obtained. The initial solution might have two or more impulses. Later, the primer vector norm and its derivative are plotted to determine the violations of the necessary conditions. Depending on that information, the addition of impulse or coast arcs can be considered [34, 35, 36]. However, these additions of impulses to the trajectory have to be done in an incremental manner. If there are multiple violations, the order of the introducing impulses can affect the final trajectory.

Application of the primer vector for determining the number of impulses on multi-gravity-assist trajectories is also demonstrated in [37]. An algorithm to optimize the number of impulses for the fuel-optimal linear impulsive rendezvous problem is proposed in [38] by utilizing the primer vector theory. Analytical solutions for impulsive elliptic out-of-plane rendezvous problems via primer vector theory are presented in [33].

Impulsive trajectories for interplanetary missions can be solved using broad-search algorithms, especially for multiple objectives, and multiple-impulse trajectories [39]. These methods consist of a large decision space that offers the flexibility of applicability to a greater variety of missions for automated trajectory search, often considering multiple flybys and V_∞ maneuvers [40, 41]. Landau [42] has developed an algorithm based on the primer vector theory for efficient maneuver placement for automated trajectory design that includes multiple gravity-assist maneuvers. The proposed primer-based maneuver-placement method does not increase

the dimension of the decision variables significantly. These automated trajectory design methods typically consist of multiple objectives and have discrete and continuous decision variables [43, 44]. Evolutionary algorithms seek the global optimal solution and do not require an initial guess, but they do not offer high-accuracy solutions for impulsive trajectories [45]. Some example studies are given in the References [46, 47, 48, 49, 50].

As an alternative method, the location and time of the impulses for an impulsive trajectory can be obtained by applying continuation-based methods. A homotopy-based and/or continuation-based approach is used for the indirect-based impulsive trajectories [31]. For instance, Zhu et al. considered a continuation procedure to be applied on the thrust parameter to obtain low-thrust solutions starting from a two-impulse Lambert solution [51]. Recently, Taheri and Junkins [4] introduced and utilized the concept of optimal switching surfaces and have shown that a bottom-up approach, leveraging continuous-thrust solutions, can be used to generate multiple-impulse minimum-Δv solutions. They performed a natural parameter continuation on the maximum thrust parameter to get a high-quality initial guess for the direct methods-based impulsive trajectory optimization tool. Another version of this approach is proposed where the optimal control problem is formulated using the acceleration to simplify the formulation, and the continuation is performed in the maximum acceleration parameter [52, 53, 54].

1.4 Current Work

This research effort investigates the multiplicity of minimum-Δv trajectories first reported in the literature for the Earth-to-Dionysus problem. The investigation of iso-impulse minimum-Δv solutions leads to an analytical Δv-allocation problem. First, a two-impulse base problem is solved. The base solution provides information on the location of what we coin as *the impulse anchor positions* and the impulse directions from the primer vector theory. We show that at the impulse anchor positions, the required impulse can be divided into multiple smaller-magnitude impulses, which leads to Δv-allocation problems. We note that all the impulses are applied in the same direction not to affect the Δv-optimality where this direction is determined

from the primer vector theory. We show that these smaller impulses inject the spacecraft into intermediate phasing orbits.

A schematic for an example heliocentric trajectory is shown in Fig. 1.1. The connecting

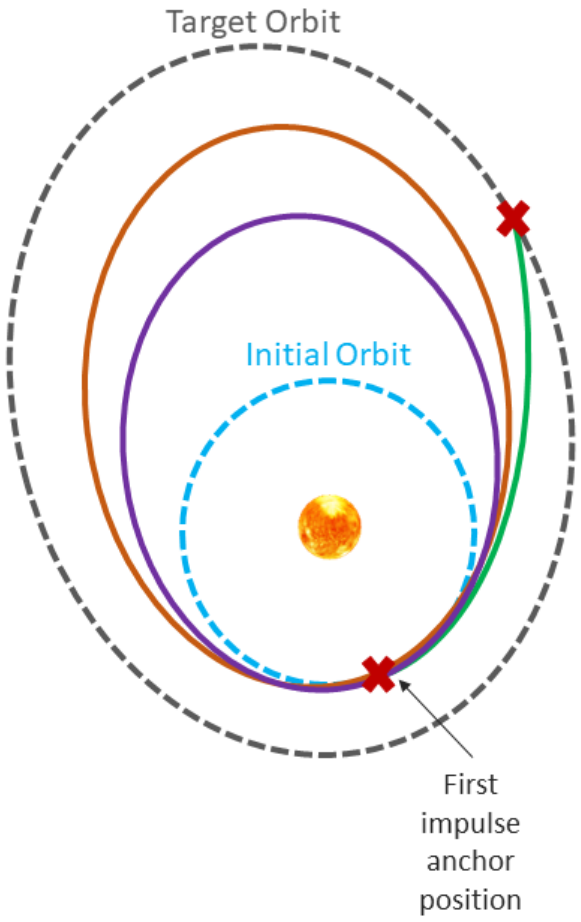

Figure 1.1: An example trajectory. Cross markers indicate impulses. Purple and orange orbits are intermediate phasing orbits. The green arc is the connecting arc generated from a two-impulse base solution. All the impulses at the first impulse anchor position are applied in the same direction.

arc (green in Fig. 1.1) is obtained from the two-impulse base solution. At the first impulse anchor position, the total impulse is divided into smaller magnitude impulses so that the orange and purple phasing orbits are added to the trajectory. In this process, the total Δv of the problem is not affected. Different number of revolutions on different segments of the trajectory creates different families of minimum-Δv iso-impulse solutions. Each family consists of infinitely many solutions. The solution to the Δv-allocation problem will result in the generation of impulsive trajectories for long-time-horizon multiple-revolution solutions. The proposed method

is generalized to prove that it is not only applicable to the Earth-Dionysus problem but also to planet-centric problems. The study also aims to answer the lower and upper bounds on the number of impulses for long-time-horizon problems. The existence of infinitely-many solutions offers flexibility for the mission design process to satisfy the constraints of the thruster since the impulses can be divided into small-magnitude impulses without the loss of Δv-optimality with the cost of increasing mission time for some of cases.

The thesis is organized as follows. In Chapter 2, the dynamical models, Lambert's problem, and primer vector theory are reviewed. In addition, the continuation-based method that is used for generating impulsive maneuvers is explained. Continuation-based methods are among the recent class of problems, and the solutions obtained using the continuation-based methods serve as the baseline solutions for comparison purposes. In Chapter 3, starting from a fundamental two-impulse solution, the generation of many multiple-impulse trajectories is explained. In Chapter 4, the analytical relations derived for generating solution envelopes are described. In Chapter 5, the results of the continuation-based method are given. Additionally, some of the trajectories belonging to different families of solutions are included, which are obtained analytically by the proposed method. Obtained solution envelopes for solution families are also shown in Chapter 5. In Chapter 6, a discussion on the upper and lower bounds of the number of impulses is presented for impulsive trajectories. In Chapter 7, a new interpretation of the primer vector for trajectories including phasing orbits is shown. Portions of the study presented in this thesis are previously published in the References [53, 55, 56].

Chapter 2

Continuation-Based Impulsive Trajectory Optimization

In this chapter, some of the fundamental methods and the dynamics of the problem are explained. Additionally, a continuation-based method to generate extremal impulsive solutions is explained. The continuation-based method utilizes a high-acceleration initial guess obtained by applying a continuation to the maximum acceleration parameter to generate impulsive trajectories [4, 52]. For spacecraft trajectory optimization using impulsive maneuvers, a hybrid method is developed based on the work presented in [36]. The hybrid method is a combination of a direct-based NLP solver and the indirect-based primer vector theory necessary conditions. We would like to emphasize that the continuation-based method is not the main contribution of this thesis. However, it allows obtaining a baseline solution for Earth-Dionysus problem and serves as an example to explain the multiplicity of the solutions.

2.1 Two-Body Dynamics and Lambert's Problem

The dynamics of the system are represented with two-body equations. Lambert's problem is solved by generating a position-continuous trajectory.

2.1.1 Two-Body Dynamics

The two-body dynamics are useful for initial analysis for trajectory generation. Higher-fidelity models incorporate the perturbing acceleration due to other bodies as third-body perturbations. The equations of motion for two-body dynamics only consider the gravitational force from the central body.

For the restricted two-body dynamics, the mass of the spacecraft is assumed to be negligible. The central body is treated as a point mass. The equations are derived in the inertial frame. Let, $\boldsymbol{r} = [x, y, z]^\top$ denote the position vector pointing from the central body to the spacecraft, using Newton's second and the universal gravitational laws, the inertial acceleration can be written as [57]:

$$\ddot{\boldsymbol{r}} = -\frac{Gm_{\text{central}}}{r^2}\frac{\boldsymbol{r}}{r}, \tag{2.1}$$

where m_{central} denotes the mass of the central body (i.e., $m_{\text{central}} = m_\odot$ for heliocentric phases of flight and $m_{\text{central}} = m_\oplus$ for Earth-centric maneuvers). In Eq. (2.1), G is the gravitational constant. Defining the gravitational parameter $\mu = Gm_{()}$ (with $m_{()}$ denoting the mass of the central body), the second-order vector-form of the differential equations can be written as

$$\ddot{\boldsymbol{r}} = -\frac{\mu}{r^3}\boldsymbol{r}. \tag{2.2}$$

2.1.2 Lambert's Problem

Lambert's problem determines the conic arc between two separate positions in space (given the time of flight between the two points). Given the initial and target positions as well as the time of flight, Lambert's problem can be solved to determine the initial and target point velocity. Thus, the required impulse magnitude can be calculated. Lambert's problem can be applied to problems such as initial orbit determination and targeting [57, 58].

In this work, Lambert's problem is used and solved as part of an inner-loop segment of an optimization algorithm to generate the connecting arc between two impulses. The discontinuity in the velocity vectors serves as the impulse at the corresponding impulse location. To ensure the continuity of the position and velocity, Lambert's problem between two consecutive impulses is solved. There exist different algorithms to solve Lambert's problem, given in References [59, 9, 60, 61, 62, 63]. In this study, Gooding's method is used, which is one of the robust, fast, and accurate solvers [61].

2.2 Earth-to-Dionysus Problem

The Earth-to-Asteroid Dionysus (Earth-Dionysus) is a long-time-horizon rendezvous-type maneuver that has become a benchmark problem for testing and validating the efficiency of new methods in solving spacecraft trajectory optimization problems [64]. In this thesis, a rendezvous-type maneuver is used to express that the initial and target points are fixed on the initial and target orbits. One of the features of the Earth-Dionysus problem is that the spacecraft maneuver correspond to a large change in the inclination. In addition, the Earth-Dionysus problem requires a maneuver from the relatively circular orbit of the Earth to the highly-elliptical orbit of asteroid Dionysus. The boundary conditions in Cartesian coordinates are given in Table 2.1. The problem is scaled using canonical units, where one astronomical unit (AU) is equal to 149.6×10^6 km and a time unit (TU) is equal to 5022750.126364 seconds. The fixed maneuver time is 3534 days. As will be shown later, since the time of flight is large for this problem, it creates a larger minimum-Δv iso-impulse solution space. Having a long-time-horizon benchmark example demonstrates the versatility of the proposed approach on a wider trade space of phasing orbit revolutions.

A comprehensive review of the minimum-fuel low-thrust and impulsive solutions for the Earth-Dionysus problem is given in Reference [4]. It is found that there exists iso-impulse (equal magnitude total impulse) solutions to the Earth-Dionysus problem with different numbers of impulses consisting of four-, five-, six-, and seven-impulse solutions. Remarkably, the magnitude of the iso-impulse is $\Delta v = 9.907425$ km/s for all the reported solutions. A peculiar feature among the iso-impulse minimum-Δv solutions is that the impulses occur at two distinct points. The impulse locations are defined here as the "impulse anchor positions." In this thesis, the significance of impulse anchor positions and how these multiple iso-impulse solutions are formed are discussed. We emphasize that the iso-impulse solutions reported in Reference [4] are obtained originally by applying a continuation-based method on the magnitude of the thrust of the propulsion system.

Table 2.1: Cartesian boundary conditions for the Earth-Dionysus problem.

Parameter	Value
Initial Position (km)	$[-3637871.082,\ 147099798.784,\ -2261.441]$
Initial Velocity (km/s)	$[-30.265,\ -0.849,\ 5.053 \times 10^{-5}]$
Final Position (km)	$[-302452014.884,\ 316097179.632,\ 82872290.075]$
Final Velocity (km/s)	$[-4.533,\ -13.110,\ 0.656]$
Time of flight (days)	3534

2.3 Acceleration-Based Switching Surfaces

The acceleration-based indirect method can be used as a first step of an impulsive trajectory optimization framework [52]. In other words, the original impulsive trajectory optimization problem can be solved initially by assuming that the spacecraft is equipped with a propulsion system that has the throttling capability and can operate over finite-time segments with a given maximum thrust acceleration level, $a_{\max}$. Upon increasing the maximum acceleration level (by a natural parameter continuation, i.e., $a_{\max} \to \infty$) we can create a dynamics-informed high-quality initial guess for impulsive trajectory optimization problems. However, one has to solve a TPBVP associated with a minimum-integral-acceleration formulation.

The key idea in the acceleration-based method is to establish a direct connection between continuous, bounded-acceleration trajectory optimization problems and minimum-Δv impulsive maneuvers [52]. This can be achieved by removing the mass, thrust magnitude, and specific impulse from the minimum-fuel problem formulation. Note that the minimum-fuel formulation was originally proposed and used in [4]. However, in the acceleration-based method, numerical continuation has to be performed on the maximum value of the acceleration, $a_{\max}$, to generate near-impulsive trajectories. From a spacecraft design point of view, it is always preferred to keep the spacecraft design generic and acceleration due to the propulsion system serves as a more fundamental quantity than thrust or mass values [65].

Let $\boldsymbol{x}(t)$ denote the vector of states and/or coordinates. Equations of motion of the spacecraft in a control-affine form can be written as

$$\dot{\boldsymbol{x}}(t) = \boldsymbol{A}(\boldsymbol{x}) + \mathbb{B}(\boldsymbol{x})\boldsymbol{a}(t), \qquad \rightarrow \qquad \dot{\boldsymbol{x}}(t) = \boldsymbol{A}(\boldsymbol{x}) + \mathbb{B}(\boldsymbol{x})a_{\max}\delta(t)\hat{\boldsymbol{\alpha}}(t), \tag{2.3}$$

where $\hat{\boldsymbol{\alpha}}(t)$ defines the acceleration steering unit vector (i.e., $||\hat{\boldsymbol{\alpha}}(t)|| = 1$). Note that the acceleration vector due to the propulsion system, $\boldsymbol{a}(t)$, is parameterized as $\boldsymbol{a}(t) = a_{\max}\delta(t)\hat{\boldsymbol{\alpha}}(t)$. This particular parametrization is adopted since it allows us to use the primer vector theory of Lawden and also modulate the acceleration magnitude through a throttle input, $\delta \in [0, 1]$, in a simple manner. The expressions for vector $\boldsymbol{A}(\boldsymbol{x})$ and matrix $\mathbb{B}(\boldsymbol{x})$ depend on the choice of coordinates/elements. In this thesis, the set of modified equinoctial elements [66] is used since it has noticeable advantages (regularity and non-singularity) in solving low-thrust trajectory optimization problems [64, 67].

A Lagrange-form cost functional for the fixed-time, minimum-acceleration problem can be defined as

$$\underset{\delta(t)\in[0,1]\ \&\ ||\hat{\boldsymbol{\alpha}}(t)||=1}{\text{minimize}} \quad J = \Delta v = \int_{t_0}^{t_f} a_{\max}\delta(t)\, dt, \tag{2.4}$$

where t_0 and t_f denote the fixed initial and final time instances, respectively, and $a_{\max}$ denotes the maximum acceleration produced by the propulsion system. It is assumed that $a_{\max}$ is fixed for each TPBVP, but its value will be used as a continuation parameter to obtain near-impulsive solutions. The admissible set of acceleration values is from a minimum value, $a_{\max,L}$, for which it is possible to find a minimum-acceleration trajectory. The upper value for $a_{\max}$ is ∞ (in theory) at which it is possible to find an actual impulsive extremal solution.

We proceed by forming the optimal control Hamiltonian associated with the cost functional given in Eq. (2.4) and the state dynamics given in Eq. (2.3) as

$$H = a_{\max}\delta(t) + \boldsymbol{\lambda}_{\boldsymbol{x}}^{\top}\left[\boldsymbol{A}(\boldsymbol{x}) + \mathbb{B}(\boldsymbol{x})a_{\max}\delta(t)\hat{\boldsymbol{\alpha}}(t)\right], \tag{2.5}$$

where $\boldsymbol{\lambda}_{\boldsymbol{x}} \in \mathbb{R}^6$ denotes the costate vector. The differential equation for the costate vector is

$$\dot{\boldsymbol{\lambda}}_{\boldsymbol{x}}(t) = -\left[\frac{\partial H}{\partial \boldsymbol{x}}\right]^{\top}. \tag{2.6}$$

Expressions for the optimal control inputs can be determined using Pontryagin's Minimum Principle and Lawden's primer vector theory as

$$\hat{\boldsymbol{\alpha}}^*(t) = -\frac{\mathbb{B}^\top \boldsymbol{\lambda}_{\boldsymbol{x}}}{\|\mathbb{B}^\top \boldsymbol{\lambda}_{\boldsymbol{x}}\|}, \qquad \delta^*(t) = \begin{cases} 1, & \text{if } S > 0, \\ \in [0,1], & \text{if } S = 0, \\ 0, & \text{if } S < 0 \end{cases} \qquad S = \left\|\mathbb{B}^\top \boldsymbol{\lambda}_{\boldsymbol{x}}\right\| - 1, \tag{2.7}$$

where $S = S(\boldsymbol{x}, \boldsymbol{\lambda}_{\boldsymbol{x}})$ denotes the acceleration switching function. It is possible for an optimal throttle solution profile to consist of singular control arcs (i.e., when $S = 0$ for one or multiple non-zero finite time intervals), however, singular control arcs are rare in space flights [68] and are ignored in this work. To alleviate the issues associated with the non-smooth bang-off-bang throttle, the hyperbolic tangent smoothing method is used [69] as

$$\delta^*(S;\rho) = \frac{1}{2}\left[1 + \tanh\left(\frac{S}{\rho}\right)\right], \tag{2.8}$$

where $\rho \in (0, \infty)$ is a smoothing parameter. Here, a numerical continuation is performed over the value of ρ. First, a relatively high value of ρ is used to solve a relatively easier solution. Then, the value of ρ is decreased gradually to make the throttle profile closer to the theoretically optimal bang-off-bang profile. Fixed-time, rendezvous-type maneuvers are considered in this paper. Thus, the spacecraft's initial and final times and states are defined. Then, the boundary conditions can be expressed as

$$\boldsymbol{\psi}_i = \boldsymbol{x}\left(t_0\right) - \boldsymbol{x}_i = \mathbf{0}, \qquad \boldsymbol{\psi}_f = \boldsymbol{x}\left(t_f\right) - \boldsymbol{x}_f = \mathbf{0}, \tag{2.9}$$

where $\boldsymbol{x}(t_f)$ is the vector of final values for the states (obtained from the numerical propagation of state dynamics); $\boldsymbol{x}_i$ and $\boldsymbol{x}_f$ denote the fixed initial and final values of the states and/or coordinates, respectively. As a result, the minimum-integral-acceleration problem is reduced to a TPBVP with the following components: state and costate differential equations given in Eqs. (2.3) and (2.6), respectively, the optimal steering unit vector given in Eq. (2.7), the optimal throttle input given in Eq. (2.8) with the switching function, S, given in Eq. (2.7), and

the terminal vector constraints given in Eq. (2.9). This two-parameter family of TPBVPs can be written as a non-linear root-solving problem as

$$\boldsymbol{\psi}_f(\boldsymbol{\lambda}_{\boldsymbol{x}}(t_0); \rho, a_{\max}) = \boldsymbol{x}\left(t_f\right) - \boldsymbol{x}_f = \mathbf{0}, \tag{2.10}$$

where $\boldsymbol{\lambda}_{\boldsymbol{x}}(t_0)$ is the unknown initial costate vector; ρ and $a_{\max}$ denote the continuation parameters that are constants for each TPBVP. For a fixed value of ρ and a relatively low value for $a_{\max}$, the resulting shooting problem is typically solved using a root-solving solver (e.g., MATLAB's `fsolve`) through multiple initial guesses for $\boldsymbol{\lambda}_{\boldsymbol{x}}(t_0)$. Upon finding a solution, a numerical continuation can be performed over the two parameters such that $\rho \to 0$ and $a_{\max} \to \infty$. The resulting solution to the two-parameter family of TPBVPs, which is a near-impulsive solution (since in practice $a_{\max} < \infty$) is used as an initial guess to an optimization procedure for finding exact impulsive solutions.

A switching surface is a by-product of the application of the continuation process. Usually, first, the ρ parameter is decreased to a sufficiently small level. Afterward, the continuation of the acceleration parameter is performed. As the TPBVP is solved for each different $a_{\max}$ parameter, each solution results in a switching function, S, that represents the bang-off-bang structure of the throttle. The time history of each S is concatenated to obtain a surface. The switching surface can provide insights into the evolution of the thrust and coast arcs, as well as the number of thrusting arcs.

2.4 Primer Vector Theory

Primer vector theory is fundamental to both impulsive and continuous-thrust problems. Primer vector theory is attributed as an indirect method, since its derivation is based on minimizing the optimal control Hamiltonian [1]. However, it can be used to evaluate the solution of a direct method or it can be combined with a direct method. The combination of the direct method and the primer vector is called the hybrid method. For continuous-time trajectory optimization problems, the direction of the acceleration vector (i.e., the control) is defined in terms of the

primer vector. For impulsive problems, the locations and times of impulses can be determined using the primer vector.

Necessary conditions for optimal impulsive trajectories were derived by Lawden in his seminal work [5] in terms of the primer vector norm and its derivative. Primer vector is defined as, $\mathbf{p}(t) = -\boldsymbol{\lambda}_v(t)$, where $\boldsymbol{\lambda}_v$ is the costate vector associated with the velocity vector. The primer vector defines the optimal direction of the impulse vector. The negative sign is due to the fact that applying Pontryagin's Minimum Principle. On an extremal trajectory, the primer vector norm should satisfy the following relation

$$\|\mathbf{p}(t)\| \leq 1, \tag{2.11}$$

where equality holds at the time of impulses. At the i-th impulse, the primer vector is a unit vector in the impulse direction

$$\mathbf{p}(t_i) = \frac{\Delta \boldsymbol{v}_i}{\Delta v_i}, \Rightarrow ||\mathbf{p}(t_i)|| = 1, \tag{2.12}$$

where $\Delta v_i = ||\Delta \boldsymbol{v}_i||$. Let $\boldsymbol{v}$ denote the velocity vector, the costate vector associated with the position vector, $\boldsymbol{\lambda}_r$, which is the derivative of the primer vector, can be obtained using the Euler-Lagrange equation written compactly as

$$\dot{\boldsymbol{\lambda}}_v^\top = -\frac{\partial H}{\partial \boldsymbol{v}} = -\boldsymbol{\lambda}_r^\top \Rightarrow \dot{\mathbf{p}}(t) = \boldsymbol{\lambda}_r(t), \tag{2.13}$$

where H denotes the Hamiltonian associated with the minimum-Δv formulation [1]. In addition to the above conditions, the primer vector and its first derivative should be continuous along an extremal trajectory [5]. The norm of the primer vector has a local maximum at the instance of an impulse. Therefore, for the intermediate impulses, its derivative should be equal to zero, which can be stated as

$$\dot{p}(t_i) = \dot{\mathbf{p}}^\top(t_i)\mathbf{p}(t_i) = 0. \tag{2.14}$$

Equation (2.14) only applies to the initial and final impulses if they are surrounded by coast arcs. Example primer vector time histories for continuous-thrust and impulsive trajectories are shown in the top and bottom subplots, respectively, in Fig. 2.1. The impulses are denoted with circles. For instance, the lower plot in Fig. 2.1 shows an extremal solution with six impulses, however, all impulses are "intermediate" impulses, and Eq. (2.14) holds at the time of impulses. The first and last impulses are preceded and followed by coast arcs. The lower plot satisfies the necessary conditions since the primer magnitude is below 1 during the coasting arcs between two impulses. However, in the upper plot, the primer magnitude exceeds the value of 1 and those regions represent the thrusting arcs.

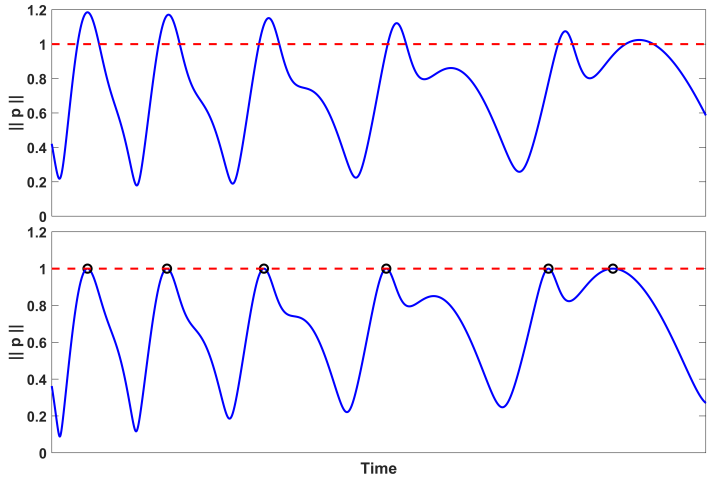

Figure 2.1: Primer vector magnitude ($\|\mathbf{p}(t)\|$) vs. time for a high-acceleration continuous thrust solution (top) and impulsive solution (bottom). Circles indicate impulses.

To evaluate the primer vector time history between two successive impulses, the state transition matrix (STM) can be used [1]. Primer vector and its time derivative can be mapped between two consecutive impulses applied at $t = t_0$ and t as

$$\begin{bmatrix} \mathbf{p}(t) \\ \dot{\mathbf{p}}(t) \end{bmatrix} = \Phi(t, t_0) \begin{bmatrix} \mathbf{p}(t_0) \\ \dot{\mathbf{p}}(t_0) \end{bmatrix}, \tag{2.15}$$

where $\Phi(t, t_0)$ denotes the STM with its derivation during a coast arc given by Glandorf [70]. The initial value of the derivative of the primer vector should be calculated. Upon defining

sub-partitions of the STM as

$$\mathbf{\Phi}(t,t_0)=\left[\begin{array}{cc}\mathbf{\Phi}_1 & \mathbf{\Phi}_2\\ \mathbf{\Phi}_3 & \mathbf{\Phi}_4\end{array}\right]_{6\times 6}, \tag{2.16}$$

it can be shown that [70]

$$\left[\begin{array}{c}\boldsymbol{\lambda}_r\left(t_0\right)\\ \boldsymbol{\lambda}_r\left(t_{\mathrm{f}}\right)\end{array}\right]=\left[\begin{array}{cc}\mathbf{\Phi}_2^{-1}\mathbf{\Phi}_1 & -\mathbf{\Phi}_2^{-1}\\ \mathbf{\Phi}_4\mathbf{\Phi}_2^{-1}\mathbf{\Phi}_1-\mathbf{\Phi}_3 & \mathbf{\Phi}_4\mathbf{\Phi}_2^{-1}\end{array}\right]\left[\begin{array}{c}\boldsymbol{\lambda}_v\left(t_0\right)\\ \boldsymbol{\lambda}_v\left(t_{\mathrm{f}}\right)\end{array}\right]. \tag{2.17}$$

Therefore, the boundary values of the derivative of the primer vector between two consecutive impulses can be determined, which can be used to plot the time histories of the primer vector magnitude and its derivative.

2.5 Impulsive Trajectory Optimization with A Hybrid Method

The hybrid method to obtain impulsive trajectories is to utilize the primer vector theory. This method combines the gradient-based optimizer with primer vector-based gradient information to improve convergence. The initial guess is important for convergence. Therefore, using the high-acceleration solution is the key step in this formulation since it is a dynamics-informed, high-resolution initial guess. In the hybrid impulsive trajectory optimization tool, there are two layers. The outer layer is a gradient-based solver that provides the position and time information of the impulses. The inner layer creates a continuous trajectory in terms of position and velocity by solving Lambert's problem and the discontinuity in the velocity becomes the required impulse.

The optimization problem for designing multiple-impulse, minimum-Δv trajectories can be stated as

$$\underset{\boldsymbol{\eta}}{\text{minimize}}\ J=\sum_{k=1}^{N}\left\|\Delta\boldsymbol{v}_k\right\|, \tag{2.18}$$

where N is the total number of impulses, $\Delta\boldsymbol{v}_k$ denotes the k-th impulse vector and $\boldsymbol{\eta}$ represents the vector of decision variables (see Eq. (2.19)). Position continuity is enforced by solving

Lambert's problem at each leg. Thus, the trajectory is prescribed to have multiple legs. Each leg represents the coasting arc between two successive impulses. The time at which an impulse occurs and the impulse position vector at that time instant are the design variables for that specific leg of the trajectory. Therefore, the vector of decision variables is

$$\boldsymbol{\eta} = \left[\begin{array}{cccccccc} t_1, & t_2, & \ldots, & t_N, & \mathbf{r}_{2+}^\top, & \mathbf{r}_{3+}^\top, & \ldots, & \mathbf{r}_{\mathrm{N-1+}}^\top \end{array} \right]^\top, \tag{2.19}$$

where t_k is the impulse time and $\mathbf{r}_{k+}$ denotes the k-th impulse position (for $k = 1, \ldots, N$). The subscript "+" represents the position just after the k-th impulse. Note that the initial and final times (t_0 and t_f, respectively) and position vectors are fixed and not included as decision variables since a fixed-time, rendezvous-type problem is considered (i.e., the Earth-Dionysus problem). If the initial position and time are design variables too, the decision variable vector is simply extended by including those variables.

The gradient of the cost with respect to decision variables is given using the primer vector and its derivative [1]. Therefore, for the initial and final coast arcs, gradients with respect to first and last impulse times and inner impulse positions and times can be calculated as

$$\begin{array}{ll} \dfrac{\partial J}{\partial t_1} = -\Delta v_1 \dot{\mathbf{p}}_1^\top \mathbf{p}_1, & \dfrac{\partial J}{\partial t_N} = -\Delta v_N \dot{\mathbf{p}}_N^\top \mathbf{p}_N, \\ \dfrac{dJ}{d\mathbf{r}_{i+}} = \dot{\mathbf{p}}_{i+}^\top - \dot{\mathbf{p}}_{i-}^\top, & \dfrac{dJ}{dt_i} = -(\dot{\mathbf{p}}_{i+}^\top \mathbf{v}_{i+} - \dot{\mathbf{p}}_{i-}^\top \mathbf{v}_{i-}), \end{array} \tag{2.20}$$

in which subscripts "$-$" and "$+$" represent the values just before and after an impulse. Also, $i = 2, \ldots, N-1$ for the inner impulses. Any NLP solver can be used to solve the optimization problem defined in Eq. (2.18) by supplying the analytical expressions for the required gradients. In this thesis, MATLAB's `fmincon` is used with the option of `user-defined` gradients. The analytic gradients obtained using Eq. (2.20) are based on the implicit satisfaction of Lawden's necessary conditions for the optimality of impulsive solutions. Since the number of impulses is known from the near-impulsive solution obtained using the procedure outlined in Section 2.3, there is no need to consider the addition of impulses or terminal coasts for fixed-time problems.

Chapter 3

Generation of Many Multiple-Impulse Minimum-Δv Trajectories

The traditional procedure for obtaining minimum-Δv impulsive trajectories using either standard methods or continuation-based optimal switching surfaces method is reviewed in Chapter 2. In this chapter, the motivation and key steps in generating many multiple-impulse, minimum-Δv trajectories are explained for the Earth-Dionysus problem, which is known to have many local minimum-fuel solutions.

For the class of fixed-time, rendezvous-type, minimum-fuel trajectories, the global solution can be obtained by enforcing the number of orbital revolutions, N_{rev}, around the Sun [4] and by investigating integer values of N_{rev}. For the Earth-Dionysus problem, four extremal multiple-impulse trajectories are reported with the same total value of $\Delta v = 9.907425$ km/s [4], but with different numbers of impulses and different N_{rev} values. The solution in Fig. 3.1 reproduces one of these extremals using the acceleration-based method reviewed in Section 2.3 where 'au' stands for the astronomical unit. However, in this thesis, a new method is proposed to generate multi-impulse, minimum-Δv solutions faster compared to continuation-based methods. The first five impulses are located at what we define as a potential "impulse anchor position." This point is common in different cases that have different numbers of revolutions [4]. The arc between two impulses is common for each solution as well as the initial and final coast arcs. The direction of the first five impulses is in the same direction in all extremal solutions. These key features set the stage for the generation of iso-Δv solutions.

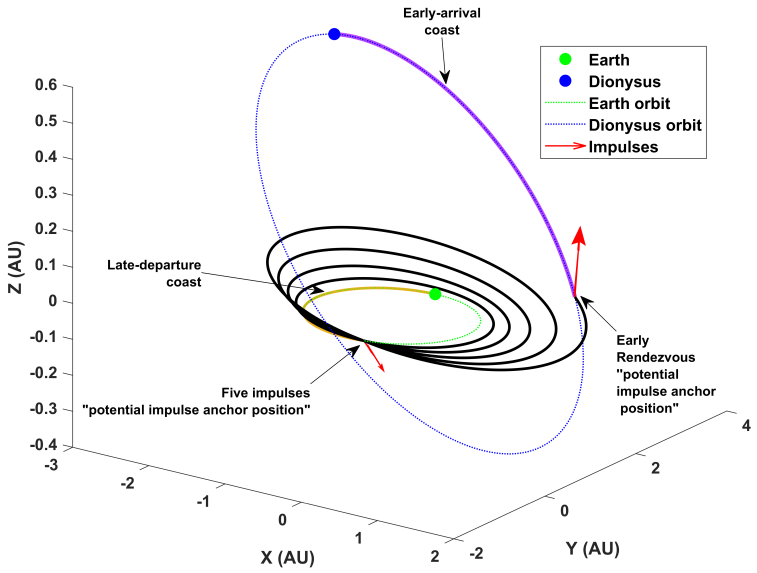

Figure 3.1: Six-impulse minimum-Δv Earth-Dionysus trajectory with $N_{\text{rev}} = 5$.

3.1 Phase-free two-impulse solution

Upon inspecting a number of multiple-revolution impulsive solutions of the Earth-Dionysus problem (see Figures 51-53 in [4]), we notice that all intermediate impulses, only appear in two locations. We determine potential impulse anchor positions at which the impulse is divided into several smaller-magnitude, same-direction impulses. For instance, in Fig. 3.1, there are two potential impulse anchor positions. Five impulses are applied at one anchor position and one impulse is applied at the other anchor position to achieve an early rendezvous. We analyze the impulse anchor position at which five impulses are applied since the magnitude of the impulse is large at that potential impulse anchor position. The procedure for determining the impulse anchor positions is given in this chapter. Therefore, as a first step of generating many multiple-impulse trajectories, we need to determine the impulse anchor positions and the connecting arc between the two potential impulse anchor positions. We choose the first position as the impulse anchor position since the magnitude of the total impulse applied at that position is higher and provides a larger solution space.

Upon analyzing the reported multiple-impulse solutions, the location of the first impulse coincides with the Earth's location, since there exists a late-departure coast. The first impulse is not applied at the specified initial time of the mission. Since all consequent impulses (except for the last impulse) are also applied at the same position, we can conclude that the intermediate impulses place the spacecraft on a number of phasing orbits that satisfy the timing constraints of the fixed-time problem. Also, in all reported impulsive solutions, the last impulse occurs at the same location on the orbit of asteroid Dionysus. This indicates that a phase-free two-impulse arc can be used to determine the time available for phasing orbits through optimizing the time of flight on the connecting arc, the location of the impulse anchor position, and the magnitude of the impulses. Then, we can add phasing orbits to the trajectory by maintaining the Δv-optimality if we keep the direction of the applied Δv indicated by the primer vector theory.

The formulation of the phase-free two-impulse problem can be stated mathematically as,

$$\underset{\theta_i,\, \theta_f,\, t_{\text{pf}}}{\text{minimize}} \quad ||\Delta \boldsymbol{v}_i|| + ||\Delta \boldsymbol{v}_f||, \tag{3.1}$$

where $\theta_i \in [0, 2\pi]$ and $\theta_f \in [0, 2\pi]$ denote the true anomaly values at the departure point from the initial orbit and at the arrival point on the final orbit, respectively, and t_{pf} is the time of flight on the phase-free transfer arc; $\Delta \boldsymbol{v}_i$ and $\Delta \boldsymbol{v}_f$ denote the initial and final impulse vectors on the phase-free arc, respectively. The parametric optimization problem, which can be solved efficiently, uses a zero-revolution formulation of Lambert's problem [59, 71]. Solving the optimization problem defined in Eq. (3.1) circumvents the step of generating switching surfaces completely. With the proposed computationally-efficient method, we can generate optimal multiple-impulsive, minimum-Δv solutions in orders of magnitude faster time compared to the acceleration-based method [53] or methods that are based on solving a continuous optimal control problem [4]. Since the phase-free two-impulse arc is part of all impulsive solutions, this phase-free two-impulse arc is the starting point to generate infinitely many multiple-impulsive minimum-Δv solutions. The initial and final coast arcs are determined from the obtained true

anomaly information (θ_i and θ_f) and the true anomaly of the Earth and Dionysus at the initial and final position.

Upon inspecting Fig. 3.1, we can conclude that for a multiple-impulse solution, the sum of the magnitudes of all $\Delta \boldsymbol{v}$ vectors except for the last one (at the rendezvous point with asteroid Dionysus) should be equal to the magnitude of the first $\Delta \boldsymbol{v}$ of the phase-free two-impulse arc. In addition, from the extremal solution, the direction of the impulses is equal for all the impulses at the impulse anchor position. Therefore, we can divide the impulse (totaling 7.521545 km/s) to introduce multiple phasing orbits to the trajectory. These phasing orbits return to the impulse anchor position after one (or multiple) revolution(s). The primer vector also cycles with the orbit and its value is equal to its final value. As a result, the next impulse primer vector points in the same direction as the previous phasing orbit or the phase-free arc. The procedure of introducing phasing orbits for generating families of solutions with three, four, and more-than-four impulses (by breaking up the total impulse at the impulse anchor position) is explained in the following sections.

3.2 Three-impulse solutions

Starting from the phase-free two-impulse arc, the addition of a single phasing orbit creates a three-impulse trajectory that satisfies the phasing time of flight (TOF) constraint. Since the total time of flight of the mission is fixed, the time that can be spent on the phasing orbit is fixed and limited. To satisfy the constraint on the time available for phasing, the following relation is written:

$$M\, T_E + N\, T_p + N_D\, T_D + N_{\text{pf}}\, T_{\text{pf}} = TOF, \tag{3.2}$$

where T_p is the orbital period of a phasing orbit, T_E is the orbital period of the Earth; M and N are the numbers of integer orbital revolutions on the Earth's orbit, and on the phasing orbit, respectively. In Eq. (3.2), TOF denotes the time available for phasing orbits (note that TOF is not the time-of-flight for the entire mission); T_D and T_{pf} denote the orbital periods of the asteroid Dionysus and the phase-free two-impulse arc; $N_D, N_{\text{pf}} \in \{0, 1, \cdots\}$ are integer number of revolutions on the Dionysus and phase-free arc.

Under the assumption that $M = N_D = N_{\text{pf}} = 0$, it is shown (in Section 5.2) that three arcs are common among all solutions, including 1) a coast arc on Earth's orbit, 2) a phase-free two-impulse arc, and 3) a coast arc on the orbit of asteroid Dionysus. The coast arcs on the Earth's and Dionysus' orbits correspond to late-departure and early-arrival coast arcs. By subtracting the times spent on these three arcs from the total mission flight time, we can obtain the remaining time of flight that can be distributed among four phases. This remaining time of flight is denoted by TOF in the right-hand side of Eq. (3.2) and throughout the manuscript. In Eq. (3.2), the only unknown is the orbital period of the phasing orbit, T_p, which can be easily determined since over a range of integer values for M and N (and the known TOF value), we can solve for T_p. Once the orbital period of the phasing orbit is determined, the needed Δv can be calculated. The phasing orbit is an intermediate step in the maneuver. Primer vector time history for the phase-free two-impulse solution shows that having two impulses at the impulse anchor positions generates an extremal solution with a minimum Δv. We apply a maneuver only when the magnitude of the primer vector becomes 1, and the primer vector defines the impulse direction. The phasing orbits are added to the trajectory by applying impulses in the same direction. This direction is obtained from the phase-free two-impulse solution primer vector. The initial value of the primer vector is the same at each impulse at the anchor position and it cycles with each orbital period of phasing orbits. Therefore, the direction of the required impulse should not change, which means that the only missing component is the magnitude of the $\Delta \boldsymbol{v}$ vector, which itself depends on the period of the phasing orbit.

Once the orbital period of the phasing orbit is determined, the phasing orbit velocity magnitude can be determined. The semi-major axis, a_p, of the phasing orbit can be obtained from the orbital period of the phasing orbit as

$$T_p = \sqrt{\frac{a_p^3}{\mu}} 2\pi, \tag{3.3}$$

where μ is the gravitational parameter of the Sun. Using the orbit energy equation, and the value of a_p, the phasing orbit velocity magnitude, $v_p = ||\boldsymbol{v}_p||$, can be obtained as

$$\mathrm{E} = \frac{v_p^2}{2} - \frac{\mu}{r} = -\frac{\mu}{2a_p}, \tag{3.4}$$

where r denotes the magnitude of the position vector of the impulse anchor position. In Fig. 3.2, schematics associated with the introduction of one phasing orbit are shown. The direction of the velocity vectors is arbitrary and shown for the purpose of clarity. Here, the red $\Delta\boldsymbol{v}$ vector is the first impulse of the phase-free two-impulse arc, which is also equivalent to the sum of all impulses in Fig. 3.1 except for the last impulse. The orange vector represents the velocity of the transfer orbit or the phase-free arc. The blue vector represents the velocity of the Earth. The impulse required to place the spacecraft on the phasing orbit is shown as $\Delta\boldsymbol{v}_1$ (dashed green vector). At the time of impulse, the velocity of the Earth, $\boldsymbol{v}_E$, is known. The $\Delta\boldsymbol{v}_1$ vector is in the direction of the total $\Delta\boldsymbol{v}$ as shown in Fig. 3.2, which is known from the phase-free two-impulse solution. Therefore, the primer vector magnitude is equal to 1 at this point and the impulse direction is known. Then, the optimal direction to apply the impulse is obtained from the primer vector information. In addition, it is graphically evident that if the direction of the $\Delta\boldsymbol{v}_1$ points in any other direction, it results in a higher total Δv. When Δv_1 is pointed in any other direction, the remaining impulse is applied in a direction that it brings the velocity to the transfer orbit velocity. The addition of those two impulses will be higher than the total $\Delta\boldsymbol{v}$. Here, the direction of the total $\Delta\boldsymbol{v}$ is drawn arbitrarily to qualitatively illustrate the ideas using representative schematics. The following relation can be formed to determine the magnitude of

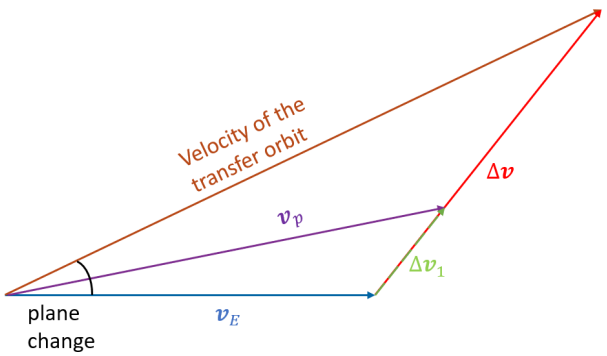

Figure 3.2: Distribution of the velocity vectors for the case with one intermediate phasing orbit.

the $\Delta \boldsymbol{v}_1$:

$$\|\boldsymbol{v}_E + \Delta \boldsymbol{v}_1\| = \|\boldsymbol{v}_p\| = v_p. \tag{3.5}$$

Since $\Delta \boldsymbol{v}_1$ is applied in the direction of the $\Delta \boldsymbol{v}$, we can express it in terms of the total $\Delta \boldsymbol{v}$ as

$$\Delta \boldsymbol{v}_1 = \alpha \Delta \boldsymbol{v}, \tag{3.6}$$

where $\alpha \in (0, 1)$ denotes the $\Delta \boldsymbol{v}$ ratio parameter. The phasing orbit periods are functions of α parameters. We can obtain the corresponding orbital period value combining Eqs. (3.3) and (3.4) as,

$$T_p = 2\pi\mu \sqrt{\left(-\frac{1}{8\left(\frac{v_p^2}{2} - \frac{\mu}{r}\right)^3} \right)}, \tag{3.7}$$

where v_p^2 is obtained from Eq. (3.5) as

$$v_p^2 = \|\boldsymbol{v}_E + \alpha \Delta \boldsymbol{v}\|^2 . \tag{3.8}$$

Parameter α can be determined by combining Eqs. (3.3), (3.7) and (3.8) as,

$$\|\boldsymbol{v}_E + \alpha \Delta \boldsymbol{v}\|^2 = -2\left(\frac{\mu^2\pi^2}{2T_p}\right)^{1/3} + \frac{2\mu}{r}, \tag{3.9}$$

which results in a quadratic equation as,

$$\boldsymbol{v}_E^\top \boldsymbol{v}_E + 2\alpha \boldsymbol{v}_E^\top \Delta \boldsymbol{v} + \alpha^2 \Delta \boldsymbol{v}^\top \Delta \boldsymbol{v} + 2\left(\frac{\mu^2\pi^2}{2T_p^2}\right)^{1/3} - \frac{2\mu}{r} = 0, \tag{3.10}$$

where the solution to α is found using the quadratic formula (with the root satisfying $\alpha \in (0, 1)$ as the solution). The sum of the roots of the quadratic equation is $-b/a$, where b is the coefficient of the linear part and a is the coefficient of the quadratic part. In Eq. (3.10), $a = \Delta \boldsymbol{v}^\top \Delta \boldsymbol{v}$, which is always positive. Also, $b = 2\boldsymbol{v}_E^\top \Delta \boldsymbol{v}$ is positive in our case. Therefore, the summation of two roots is always negative. This means that either both of the roots are negative or one of them is positive and one of them is negative with greater absolute value.

Therefore, the positive root is the only feasible solution. As a result, the problem of determining the velocity (to place the spacecraft on one phasing orbit) is solved analytically. The value of T_p can be determined from Eq. (3.2) and using T_p, α parameter is calculated by solving Eq. (3.10). Then, a feasible solution is obtained if $\alpha \in (0, 1)$.

Another approach is first a feasible α is chosen in between (0, 1) range. The corresponding T_p is calculated using Eq. (3.7). Then, the feasibility of the solution is verified by checking the constraint in Eq. (3.2).

Once the value of α is determined, the required velocity change is known. The remaining $\Delta\boldsymbol{v}$ vector (i.e., $\Delta\boldsymbol{v} - \Delta\boldsymbol{v}_1$) is applied to inject the spacecraft on the phase-free arc toward asteroid Dionysus. The last impulse, required to rendezvous with asteroid Dionysus, is the second impulse of the phase-free two-impulse arc. All analyses and discussions are related to the first impulse of the phase-free two-impulse solution at the location of the impulse anchor position (see Fig. 3.1).

3.3 Four-impulse solutions

Four-impulse solutions add one more unknown to Eq. (3.2) by introducing one more phasing orbit to the trajectory. The new relation between phasing orbits' and Earth's orbital periods can be written as,

$$N_1 T_1(\alpha_1) + N_2 T_2(\alpha_2) + M T_E + N_D\, T_D + N_{\text{pf}}\, T_{\text{pf}} = TOF, \tag{3.11}$$

where N_1 and N_2 are the (integer) number of orbital revolutions on the first and second phasing orbits; T_1 and T_2 are orbital periods of the first and second phasing orbits, which are expressed as functions of α_1 and α_2. This is the case in which another phasing orbit is added to the schematics shown in Fig. 3.2 and the respective relations between the velocity vectors are depicted in Fig. 3.3. The $\Delta\boldsymbol{v}$ required for the second phasing orbit is $\Delta\boldsymbol{v}_2$ added to the Earth's velocity vector, $\boldsymbol{v}_E$. Discussion on the direction of the impulses explained in Section 3.2 also applies for every case when phasing orbits are added to the trajectory. Therefore, $\Delta\boldsymbol{v}_1$, $\Delta\boldsymbol{v}_2$ and $\Delta\boldsymbol{v}$ should be in the same direction for obtaining minimum-Δv solutions. Geometrically, as

shown in Fig. 3.3b, when the required impulses are not aligned with the $\Delta \boldsymbol{v}$, the total impulse will be higher. In Fig. 3.3b, it is geometrically evident that $\Delta \boldsymbol{v}_1 + \Delta \boldsymbol{v}_2 + \Delta \boldsymbol{v}_3 > \Delta \boldsymbol{v}$. Also, $\Delta \boldsymbol{v}$ vectors are drawn slightly off to make them appear distinctly. The constraints on parameters

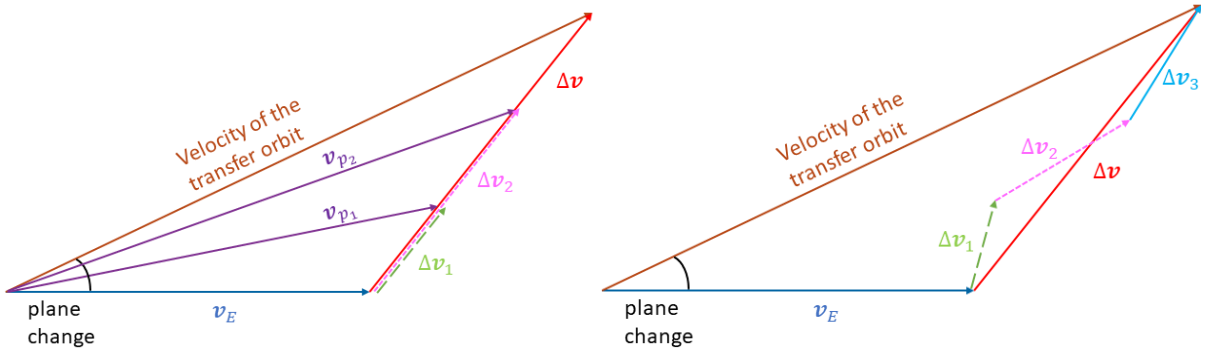

(a) Impulses are aligned with $\Delta \boldsymbol{v}$ (b) Impulses are not aligned with $\Delta \boldsymbol{v}$

Figure 3.3: Schematic for the addition of two intermediate phasing orbits.

are listed as,

$$0 < \alpha_1 < \alpha_2 < 1, \quad T_1 > 0, \; T_2 > 0, \tag{3.12}$$

where it is also evident in Fig. 3.3 that $\alpha_2 > \alpha_1$. Since the system is under-determined (with one constraint, Eq. (3.11), but two unknowns, α_1 and α_2), there exist infinitely many solutions satisfying the constraints of the problem. Infinitely-many solutions are equally optimal in terms of the total Δv. We define these solutions as iso-impulse solutions. It means they all require the exact same amount of total Δv. However, the distribution of the impulse magnitude is different for each intermediate impulse for introducing phasing orbits.

We can discretize the α_1 parameter in the range $[0, 1]$ and calculate the corresponding T_1 value from Eq. (3.7), and solve for α_2 using Eq. (3.11). More explicitly, T_2 is obtained from Eq. (3.11) as

$$T_2(\alpha_2) = (TOF - MT_E - N_1 T_1(\alpha_1) - N_D T_D - N_{\text{pf}} T_{\text{pf}})/N_2. \tag{3.13}$$

When the value of T_2 is determined, α_2 can also be determined by solving Eq. (3.10). Then, the α_1 and α_2 satisfying Eq. (3.12) are feasible solutions.

3.4 General solutions with more than four impulses

Impulsive solutions can be generalized to problems with more phasing orbits. For each case, one more phasing orbit will be added to the trajectory, which only changes the number of constraints. The equality constraint on the time available for phasing (TOF) can be generalized as,

$$\sum_{k=1}^{n_p} N_k T_k + M T_E + N_D\, T_D + N_{\text{pf}}\, T_{\text{pf}} = TOF, \tag{3.14}$$

where n_p represents the number of intermediate phasing orbits. Generalizing the equality constraint for any transfer between an initial and target orbit,

$$\sum_{k=1}^{n_p} N_k T_k + N_0 T_0 + N_f\, T_f + N_{\text{pf}}\, T_{\text{pf}} = TOF, \tag{3.15}$$

where N_0 and T_0 are the integer number of revolutions and the orbital period of the initial orbit; N_f and T_f are for the final orbit. Therefore, all of the equations are valid and general when T_E become T_0 and T_D become T_f. Similarly for the integer number of revolutions, M become N_0 and N_D become N_f. Inequality constraints for the general solution can be defined as,

$$0 < \alpha_1 < \cdots < \alpha_{n_p} < 1, \qquad T_i > 0, \qquad \text{for} \quad i = 1, \ldots, n_p, \tag{3.16}$$

where T_i denotes orbital period of the i-th phasing orbit. The analytical approach can be generalized by discretizing $\alpha_1, \cdots, \alpha_{(n_p-1)}$ in $[0, 1]$ range to solve for corresponding T_j for $j = 1, \cdots, (n_p - 1)$ using Eq. (3.7). Then, T_{n_p} is determined from Eq. (3.14). From T_{n_p} information, the quadratic equation is solved to obtain α_{n_p} as,

$$\boldsymbol{v}_E^\top \boldsymbol{v}_E + 2\alpha_{n_p} \boldsymbol{v}_E^\top \Delta\boldsymbol{v} + \alpha_{n_p}^2 \Delta\boldsymbol{v}^\top \Delta\boldsymbol{v} + 2\left(\frac{\mu^2\pi^2}{2T_{n_p}^2}\right)^{1/3} - \frac{2\mu}{r} = 0. \tag{3.17}$$

where there exists two solutions for α_{n_p}. The solution in $[0, 1]$ is chosen, as we explained in Section 3.2.

The complexity of the problem increases with the resolution of discretization of α parameters, and with the total number of phasing orbits when we want to generate all solution spaces for each combination of N_k and M values. However, we can actually solve for boundaries of the solution spaces to have a general representation of the solution spaces, as we will present the details in Chapter 4.

On the other hand, if the goal is to check whether there exist infinitely many solutions for a particular combination of N_k, M parameters, the inequality that characterizes feasible solutions can be written as,

$$T(\alpha = 0) \leq T = \frac{TOF - N_D T_D - N_{\text{pf}} T_{\text{pf}} - M T_E}{\sum_{k=1}^{n_p} N_k} \leq T(\alpha = 1), \tag{3.18}$$

where $T(\alpha = 0)$ is the minimum value of orbital period and $T(\alpha = 1)$ is the maximum orbital period of the phasing orbits. When $\sum_{k=1}^{n_p} N_k = 0$, there is no phasing orbit on the resulting trajectory. Therefore, phasing time, TOF, can be spent on Earth's orbit, Dionysus, or the phase-free two-impulse arc orbit. Equation (3.18) is derived based on one extreme case (within the family of feasible solutions) in which all intermediate phasing orbits will have the same orbital period value. In other words, if the inequalities in Eq. (3.18) are violated, the considered combination of M and N_k values (for $k \geq 1$ and $\sum_{k=1}^{n_p} N_k \neq 0$) has no feasible solution (see Section 4 for details on the family of solutions).

To generate the remaining segments of the trajectory, the remaining impulse is applied at the first impulse anchor position, which is calculated as $\Delta v - \alpha_{n_p} \Delta v$. This last impulse puts the spacecraft into the phase-free arc. As the time of flight spend on the phase-free arc is obtained by the solution of the two-impulse problem, one can propagate the Keplerian motion. At the end of the arc, the last impulse is applied to match the velocity of the target body, such as the Dionysus.

Chapter 4

Generation of Solution Envelopes for the Family of Solutions

It is possible to perform a systematic study based on the discretization of the α_i (for $i \in \{1, \cdots, n_p\}$) values to obtain a complete set of solutions for each combination of M, N_i (for $i \geq 1$), N_D and N_{pf} values. This systematic study is actually made possible due to the algebraic nature of the $\Delta\boldsymbol{v}-$allocation problems.

The most general way to obtain solution envelopes for different families of solutions is by calculating the minimum and maximum values of the orbital period values for each phasing orbit. This way, the corners of the solution envelope can be determined to gain insights on the solution space and relations between orbital periods of the phasing orbits. Then, the minimum and maximum values of orbital periods when the first phasing orbit period is $T(\alpha = 0)$ is

$$\begin{aligned} T_{s,\text{min}} &= T_E = 365.25 \text{ days}, \\ T_{n_p,\text{min}} &= \frac{TOF - N_1 T_{1,\text{min}}}{\sum_{k=2}^{n_p} N_k}, \\ T_{n_p,\text{max}} &= \frac{TOF - \sum_{k=1}^{n_p-1} N_k T_{k,\text{min}}}{N_{n_p}}, \\ T_{1,\text{max}} &= \frac{TOF}{\sum_{k=1}^{n_p} N_k}, \\ T_{m,\text{max}} &= \frac{TOF - \sum_{k=1}^{m-1} N_k T_{k,\text{min}}}{\sum_{k=m}^{n_p} N_k}, \end{aligned} \tag{4.1}$$

for $s = 1, \cdots, (n_p - 1)$ and $m = 2, \cdots, (n_p - 1)$. If $T_{n_p,\text{max}} > T(\alpha = 1)$, then the upper bound of T_{n_p} is equal to the maximum value of orbital periods, $T(\alpha = 1)$. We set $T_{n_p,\text{max}} = T(\alpha = 1)$ and solve for the additional corner that corresponds to the case $T_{n_p-1} = T_1$ and $T_{n_p} = T(\alpha = 1)$:

$$T_1 = T_{n_p-1} = \frac{TOF - N_{n_p} T_{n_p,\text{max}}}{\sum_{k=1}^{n_p-1} N_k}. \tag{4.2}$$

In the case where there exists an additional corner (as corner '4' in Fig. 5.18b), the minimum value of $T_{n_p-1} \neq T_E$. Therefore, $T_{n_p-1,\text{min}}$ and $T_{n_p-1,\text{max}}$ are calculated as

$$T_{n_p-1,\text{max}} = \frac{TOF - \sum_{k=1}^{n_p-2} N_k T_{k,\text{min}}}{\sum_{k=n_p-1}^{n_p} N_k}, \quad T_{n_p-1,\text{min}} = \frac{TOF - N_{n_p} T_{n_p,\text{max}} - N_1 T_{1,\text{min}}}{\sum_{k=2}^{n_p-1} N_k}. \tag{4.3}$$

Finally, the bifurcation point, where all the orbital periods are equal, is determined $T_{1,\cdots,n_p} = TOF/n_p$. As a result, we are able to determine the corner points that create these solution regions analytically. The application of the solution envelope calculations are explained in Section 4. We emphasize that these solution envelopes are useful for understanding the ranges of the orbital periods, which can be related to the required impulse information. If we know the orbital period, we can calculate the α parameter to obtain the required impulse. The solution envelopes obtained for the Earth-Dionysus problem are presented in Section 5.5.

Chapter 5

Results

The results obtained for the defined methods in the previous chapters are presented in this chapter. First, the application of the continuation-based method to generate initial guess for a hybrid impulsive trajectory optimization method is shown for the Earth-Dionysus problem in Section 5.1. Then, infinitely many iso-impulse solutions are given with the proposed analytical Δv-allocation method in Section 5.2. To generalize the method, GTO-GEO, and LEO-GEO problems are solved in Section 5.3 and Section 5.4. The generated solution envelopes for the Earth-Dionysus problem are presented in Section 5.5.

5.1 Continuation-Based Impulsive Trajectory Solution

5.1.1 A Near-Impulsive Solution

The fixed boundary values on the position and velocity vectors for the Earth-Dionysus problem are given in Table 2.1. The problem is scaled using canonical units where one astronomical unit (au) is equal to 149.6×10^6 km and a time unit (TU) is equal to 5022750.126364 seconds. To generate the near-impulsive solution, first, the corresponding minimum acceleration problem is solved using a single-shooting scheme [52]. Numerical continuation is performed over the smoothing parameter to obtain a solution with a particular value for $a_{\max}$. The maximum acceleration value is increased until there is no significant improvement in the total Δv value. Thus, the near-impulsive solution is obtained at this "relatively high" acceleration value.

The acceleration switching surface for a range of acceleration values is shown in Fig. 5.1, where S represents the switching function associated with the acceleration [52]. The red-colored switching function corresponds to the smallest value for $a_{\max}$ for which the entire switching function is positive (i.e., no switching occurs in the acceleration throttle profile). As the acceleration parameter, $a_{\max}$, is increased gradually, the switching function is pushed below the $S = 0$ plane (cyan-colored plane). This means that the duration of the acceleration arcs gets smaller. At high values of $a_{\max}$, the duration of acceleration arcs becomes small, which is closest to the impulsive maneuvers. Also, terminal coasts (before the first impulse and after the last impulse) are evident in the switching surface.

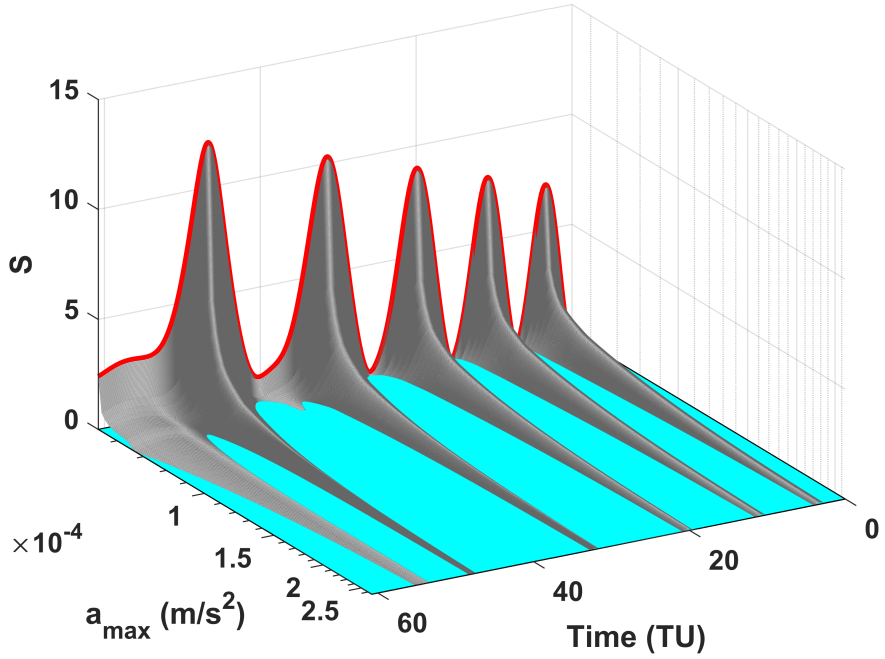

Figure 5.1: Switching surface for the Earth-Dionysus problem with $N_{\text{rev}} = 5$ generated using the acceleration-based method.

Figure 5.2a shows the trajectory for $a_{\max} = 2.66 \times 10^{-4}$ m/s^2 where the thrust arcs are shown with purple arrows. The yellow colored path is the obtained trajectory. Dashed blue and black orbits are the Earth's and Dionysus' orbits, respectively. Thrusting duration got smaller compared to the low-acceleration solutions. Also, *late-departure* and *early-arrival* arcs, introduced in [4], can be observed. First, five thrust arcs are concentrated at the perihelion

(when the spacecraft is on the closest point of the orbit to the Sun) of the intermediate quasi-elliptical orbits. This solution gives information about the impulsive solution too. It is expected to have impulse locations closer to these thrust arcs. Using the steps outlined in Section 2.4 primer vector time history of the near-impulsive solution is plotted in Fig. 5.2b. The largest value of primer vector time history is 1.08. Since it only exceeds the unity by a small value, this solution qualifies to be a high-resolution initial guess for obtaining an impulsive solution.

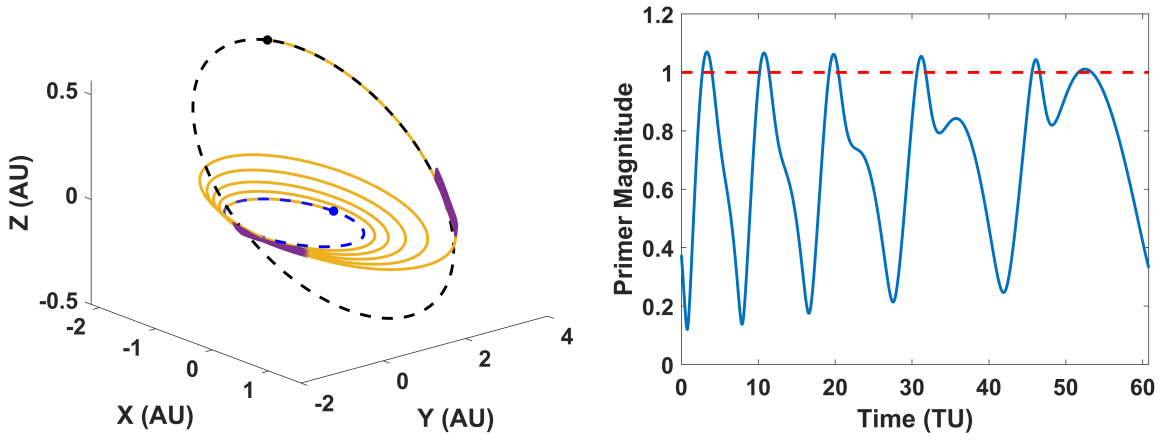

(a) (b)

Figure 5.2: **a**) Near-impulsive solution for $a_{\max} = 2.66 \times 10^{-4}$ m/s^2. **b**) Primer vector magnitude time history for the same near-impulsive solution.

5.1.2 A Multiple-Impulse Solution

The near-impulsive solution reported in the previous section is used as an initial guess to obtain the exact impulsive solution according to the optimization methodology outlined in Section 2. The impulsive solution is shown in Fig. 5.3. This trajectory is the exact same trajectory, shown in Fig. 5.10a. Thus, the proposed method is able to generate this trajectory without going through the steps of the continuation-based method. The cross markers represent the location of the impulses. Each colored orbit is the intermediate orbit. The initial and terminal coast arcs are shown in light blue and dark red.

The primer vector magnitude and the derivative of its magnitude (see Eq. (2.17)) are plotted versus time in Fig. 5.4. Circles indicates the impulses. The color of the primer magnitude and its derivative is the same with the associated segment of the trajectory given in Fig. 5.3.

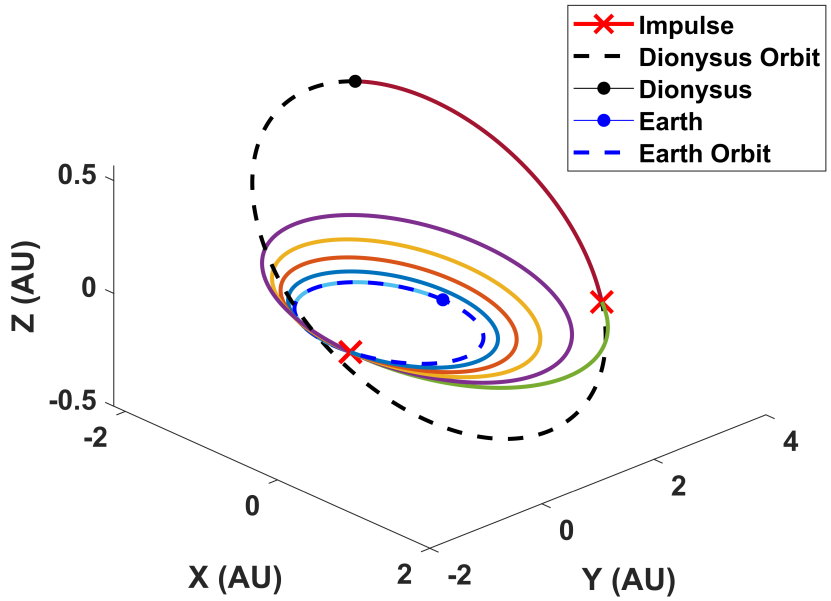

Figure 5.3: Minimum-Δv trajectory for the Earth-Dionysus problem with $N_{\text{rev}} = 5$. X marker denotes the location of impulses.

When the near-impulsive solution's primer vector magnitude and the current plots are compared, the necessary conditions are successfully satisfied. Circles indicate impulses in the plots. At the impulse positions, primer vector magnitude has a local maxima at unity. Also, for intermediate impulses (which include all the impulses for this solution), the derivative of the norm of the primer vector is continuous, and $\dot{p} = 0$ is satisfied. The total Δv value matches the known optimal solution, i.e., $\Delta v = 9.907425$ km/s reported in [4]. It is evident that the first five impulses are approximately at the same position as seen in the near-impulsive solution shown in Fig. 5.2a. Thus, impulses are concentrated at two distinct locations. Location of the impulses suggests that these two separate impulse positions are also the impulse positions for a phase-free two-impulse Lambert arc with the same total Δv.

5.2 Infinitely Many Iso-impulse Solutions

Results of continuation-based methods lead to a number of key observations that paved the way to generate the iso-impulse solutions. Recall that the impulses only appear in two locations (see Fig. 3.1). Upon solving the phase-free two-impulse problem, given in Eq. (3.1), the time of flight on the Lambert arc is 348.46 days. The magnitude of the first Δv is equal to 7.521545

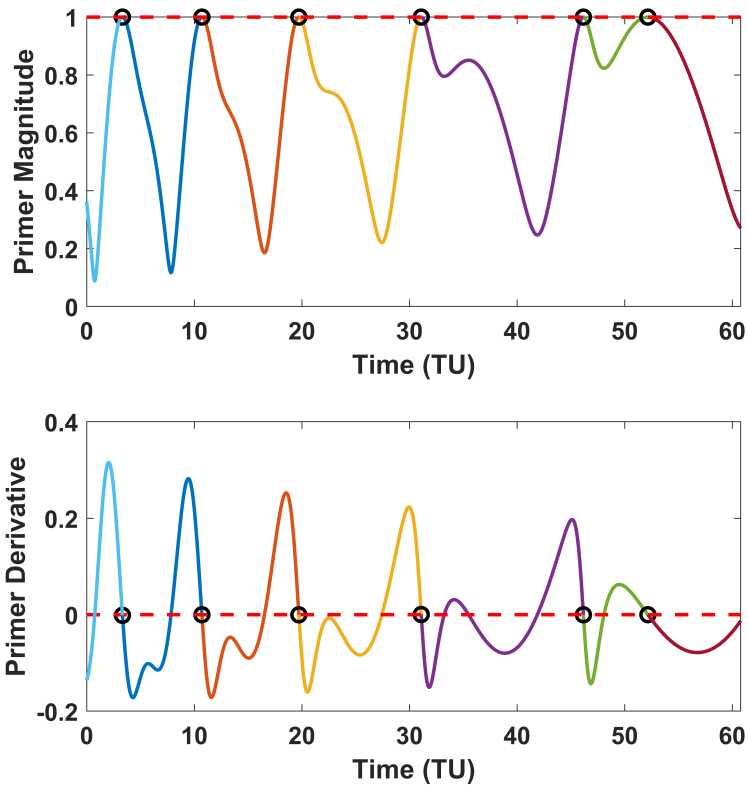

Figure 5.4: Primer vector norm and $\dot{p}$ vs. time for the Earth-Dionysus problem with $N_{\text{rev}} = 5$.

km/s and the magnitude of the second Δv is equal to 2.38588 km/s. The solution of the phase-free problem determines the initial and final true anomaly of the impulses, $\theta_i = 179.27°$ and $\theta_f = 149.20°$. We also know the true anomalies of Earth and Dionysus at the beginning and end of the mission from the boundary values given in Table 2.1. Thus, we can calculate the times spent on the coast arcs. Projection of the coast arcs on the Earth's and Dionysus' orbits and the phase-free two-impulse solution onto the $x - y$ plane (the 2D view) is shown in Fig. 5.5a. The locations of impulses are denoted with "X" markers. The initial and target orbit are shon with dashed blue and black orbits. The inital and terminal coast arcs shown in light blue and green. The phase-free connecting arc is shown in yellow. The location of the Earth and the Dionysus are shown with blue and black dot markers. The primer vector magnitude vs. time for the phase-free trajectory is plotted in Fig. 5.6. The circles indicate the location of impulses where the primer magnitude stays below 1 during the coasting between impulses and it is equal to 1 at the impulse locations. Thus, the phase-free trajectory is an extremal solution.

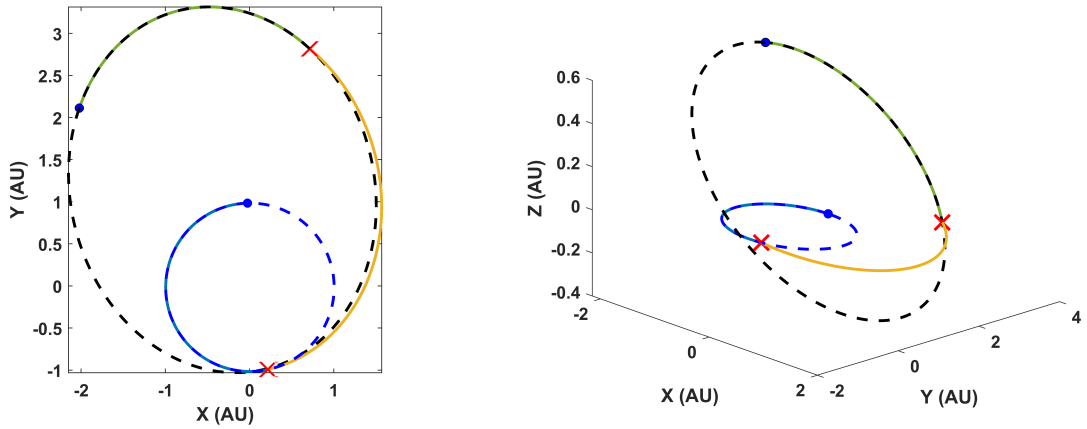

(a) Two-dimensional view of the trajectory

(b) Three-dimensional view of the trajectory

Figure 5.5: Phase-free two-impulse, minimum-ΔV solution. X marker denotes the location of impulses.

Now, we can characterize the three main coast phases. A coast arc of approximately 193.24 days on the Earth's orbit (solid blue line) and a coast arc of approximately 501.81 days on Dionysus' orbit (solid green line) and a time of flight of $t_{\text{pf}} = 348.46$ days on the phase-free two-impulse arc are common among all impulsive solutions. Thus, a difference in the timing of $TOF = 3534 - 1043.51 = 2490.48$ days is available to be distributed among several orbits.

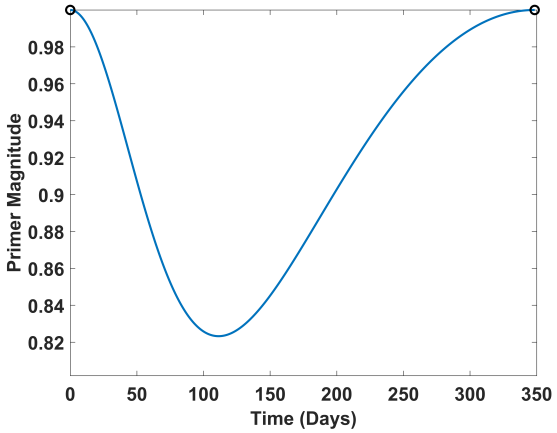

Figure 5.6: Primer vector magnitude vs. time for the phase-free two-impulse solution.

Here, $193.24 + 348.46 + 501.81 = 1043.51$ days, and 3534 days is the total time of flight of the original problem (see Table 2.1).

If we consider a standard two-impulse Lambert problem (from Earth to asteroid Dionysus) with the decision variables being the coast times on the Earth and Dionysus orbits and solve a two-impulse, minimum-Δv problem, the value of the required total Δv will be greater than the $\Delta v = 9.907425$ km/s since we have formulated a phase-constrained problem. There is no *phase-constrained* two-impulse solution with a total impulse equal to or less than $\Delta v = 9.907425$ km/s.

The main reason for the existence of the different multiple-impulse local minima (first reported in [4]) is that we can insert a number of phasing orbits that take up the missing $TOF = 2490.48$ days. To be more precise, the time can be spent on 1) Earth's orbit, 2) a number of phasing orbits, 3) the phase-free arc, and 4) the orbit of asteroid Dionysus. This is stated as a TOF constraint in Eq. (3.14). For the case of phasing orbits, the unknown number of phasing orbits breaks up the initial 7.521545 km/s impulse (shown as a red $\Delta \boldsymbol{v}$ vector in Fig. 3.2) into many minor impulsive maneuvers. However, the sum of the impulses is equal to the same total $\Delta v = 9.907425$ km/s. In essence, this step can be viewed as a Δv-allocation problem in which one can consider many opportunities to distribute the first $\Delta v = 7.521545$ km/s among a to-be-determined number of phasing orbits. In the remainder of this section, we only present a few important solutions for a number of combinations of M, N, N_D and N_{pf} values.

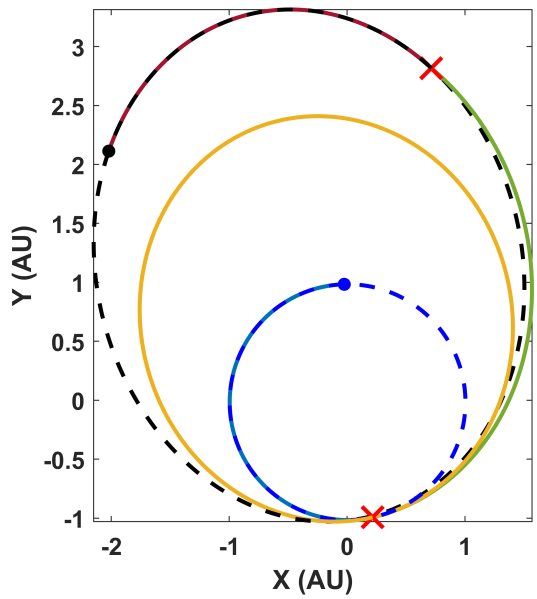

(a) $M = 0, N_1 = 3$

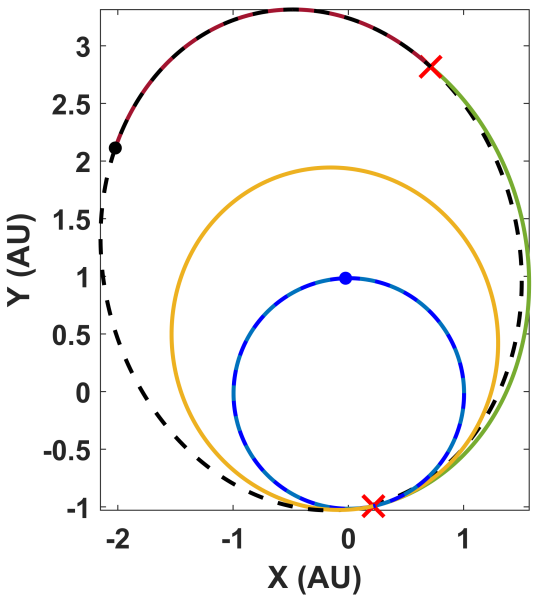

(b) $M = 5, N_1 = 1$

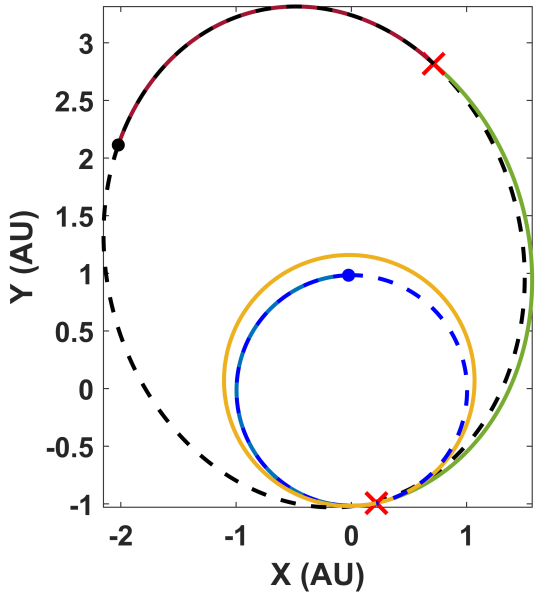

(c) $M = 0, N_1 = 6$

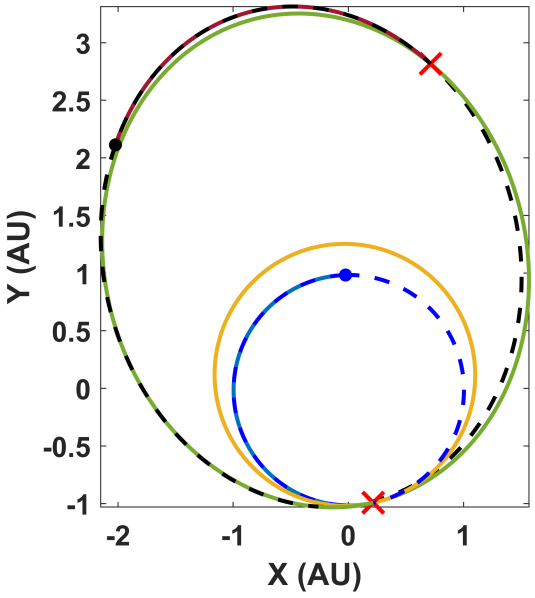

(d) $M = 0, N_1 = 3, N_{\text{pf}} = 1$

Figure 5.7: Three-impulse trajectories with **a**) three revolutions on a phasing orbit; **b**) five revolutions on the Earth's orbit and one revolution on a phasing orbit; **c**) six revolutions on a phasing orbit; **d**) three revolutions on a phasing orbit and one revolution on the phase-free leg of the trajectory. X marker denotes the location of impulses.

Three-impulse families of solutions only have one phasing orbit, which breaks up the first $\Delta v = 7.521545$ km/s into two impulses. In all trajectory plots; Earth's and Dionysus' orbits are shown with blue and black dashed orbits. Impulses are denoted with red cross markers. The location of the Earth and the Dionysus are shown at the initial and final time with blue and black dot markers. Following the steps in Section 3.2, some of the three-impulse solutions are shown in Fig. 5.7. For all impulsive solutions, the total impulse value matches the known optimal value (9.907425 km/s). Phasing orbits are shown in yellow. In Fig. 5.7a, the spacecraft makes three revolutions on the phasing orbit to take up the $TOF = 2490.48$ days with an orbital period of 830.16 days. When Earth revolutions are added, as shown in Fig. 5.7b, the time spent on the phasing orbit is reduced. Thus, the phasing orbit in Fig. 5.7b has a period of 664.23 days, and the spacecraft makes one revolution around the Sun on the phasing orbit. In Fig. 5.7c, a solution with zero revolution on the Earth's orbit is shown, whereas six revolutions on the phasing orbit occur. Comparing the trajectories in Figs. 5.7c and 5.7a, it is visible that the period of the phasing orbit gets shorter than the case with a smaller number of revolutions on the phasing orbit.

A second important family of solutions corresponds to those trajectories that make multiple revolutions on the orbit corresponding to the phase-free two-impulse arc (i.e., when $N_{\text{pf}} \neq 0$). For instance, in Fig. 5.7d, we have $N_{\text{pf}} = 1$. According to Eq. (3.14), $TOF = 2490.48 - 1161.47 = 1329.01$ days, which is different from the previous cases with $TOF = 2490.48$ days. The orbital period associated with the phase-free two-impulse arc is $T_{\text{pf}} = 1161.47$ days. The phasing orbit has three revolutions with an orbital period of 443.00 days. In total, 26 three-impulses families were obtained based on different combinations of M and N_1 values: 6 solutions with four revolutions, 9 solutions with five revolutions, 5 solutions with six revolutions, and 6 solutions with seven revolutions.

Four-impulse solutions that consist of two phasing orbits are shown in Fig. 5.8 with yellow and green colors. Another important family of solutions is plotted in Fig. 5.8a, where the $TOF = 2490.48 - 1191.88 = 1298.60$ days since $N_D = 1$ with the orbital period of Dionysus equal to $T_D = 1191.88$ days. In Fig. 5.8a, the first phasing orbit period is close to the Earth's orbit period, since the first $\Delta \boldsymbol{v}$ is significantly small. The rest of the trajectories in Fig. 5.8

have a phasing time equal to $TOF = 2490.48$ days. In Fig. 5.8b, the second phasing orbit period is more prominent and has two revolutions, resulting in the first phasing orbit having a shorter period. Fig. 5.8c shows that when one Earth revolution is added, both phasing orbits' periods get smaller. Looking at Fig. 5.8d, having more revolutions on both phasing orbits leads to having the shortest period among the plots shown here. In total, 42 different four-impulse families are obtained based on feasible combinations of M, N_i (for $i \in \{1, 2\}$), $N_D \in \{0, 1\}$ and $N_{\text{pf}} \in \{0, 1\}$ values.

Two five-impulse solutions with three phasing orbits are shown in Fig. 5.9 with yellow, green and red colors. In Fig. 5.9a, the first impulse required to transfer to the first phasing orbit is a relatively small impulse compared to the rest of the impulses. Thus, this first phasing orbit is close to the Earth's orbit. Four revolutions on this orbit do not take up much time. In Fig. 5.9b, phasing orbits are more evenly distributed along the trajectory than in the previous solution. Also, two revolutions occur on the Earth's orbit. In total, 37 different five-impulse families are obtained based on feasible combinations of M and N_i (for $i \in \{1, 2, 3\}$) values.

Two six-impulse solutions are plotted in Fig. 5.10 with yellow, green, red and orange colors. Both trajectories do not have any revolutions on the Earth's orbit. Inner phasing orbits are uniformly distributed along the trajectory, gradually increasing the orbit inclination. In Fig. 5.10b, the spacecraft stays closer to the Earth's orbit by performing minuscule impulses. In total, 21 different six-impulse families are obtained based on feasible combinations of M and N_i (for $i \in \{1, 2, 3, 4\}$) values.

Seven-impulse trajectories consist of five phasing orbits, which decreases the total possibilities of multiple revolutions on the phasing orbits. All solutions have either one or two revolutions on their phasing orbits. Two of the solutions are shown in Fig. 5.11 with phasing orbits having yellow, green, red, orange and purple colors. The first solution is presented in Fig. 5.11a. Similar to the six-impulse solution shown in Fig. 5.10a, this trajectory also has phasing orbits with increasing values for both periods and the semi-major axis. In Fig. 5.11b, the first four phasing orbits have periods closer to each other. This closeness results in the first four impulse values also being smaller compared to the last phasing orbit. Additionally, this solution has one Earth revolution that decreases the time spent on the phasing orbits. In

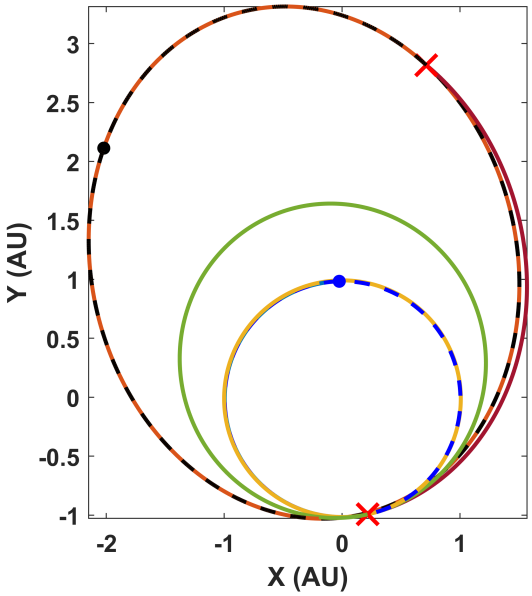

(a) $M = 0, N_1 = 2, N_2 = 1, N_D = 1$

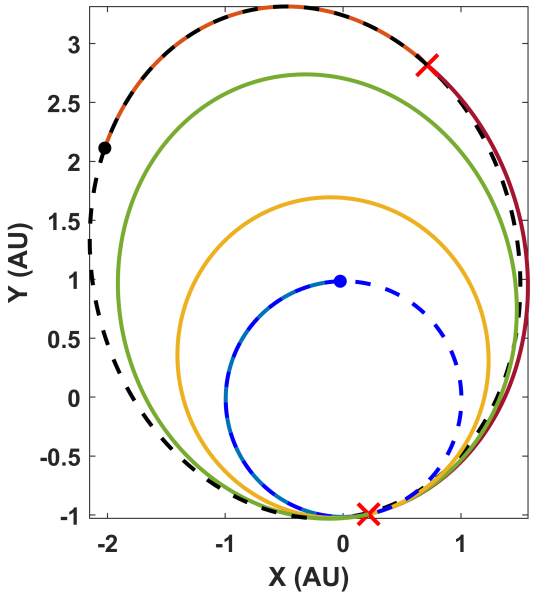

(b) $M = 0, N_1 = 1, N_2 = 2$

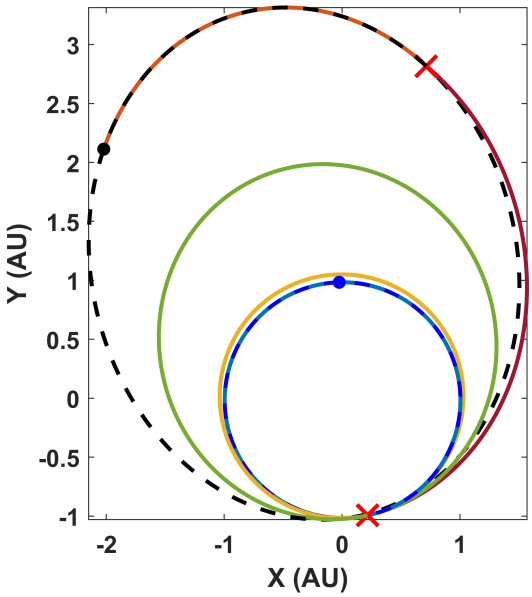

(c) $M = 1, N_1 = 2, N_2 = 2$

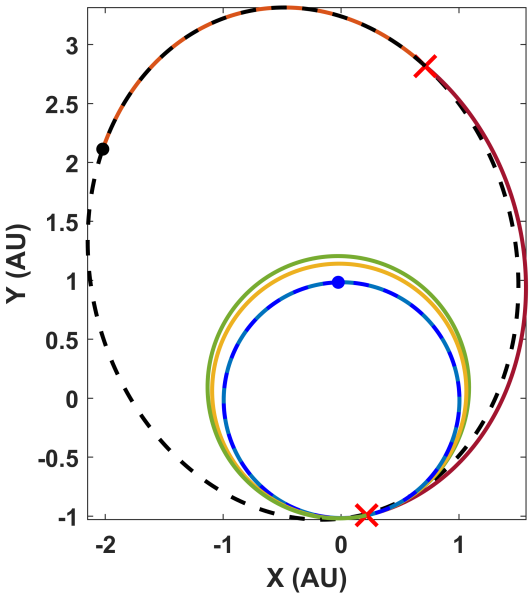

(d) $M = 1, N_1 = 1, N_2 = 4$

Figure 5.8: Four-impulse trajectories with **a**) one revolution on both phasing orbits; **b**) two revolutions on the first and one revolution on the second phasing orbit; **c**) two revolutions on both phasing orbits, and one revolution on the Earth's orbit; **d**) one and four revolutions on the two phasing orbits, and one revolution on the Earth's orbit. X marker denotes the location of impulses.

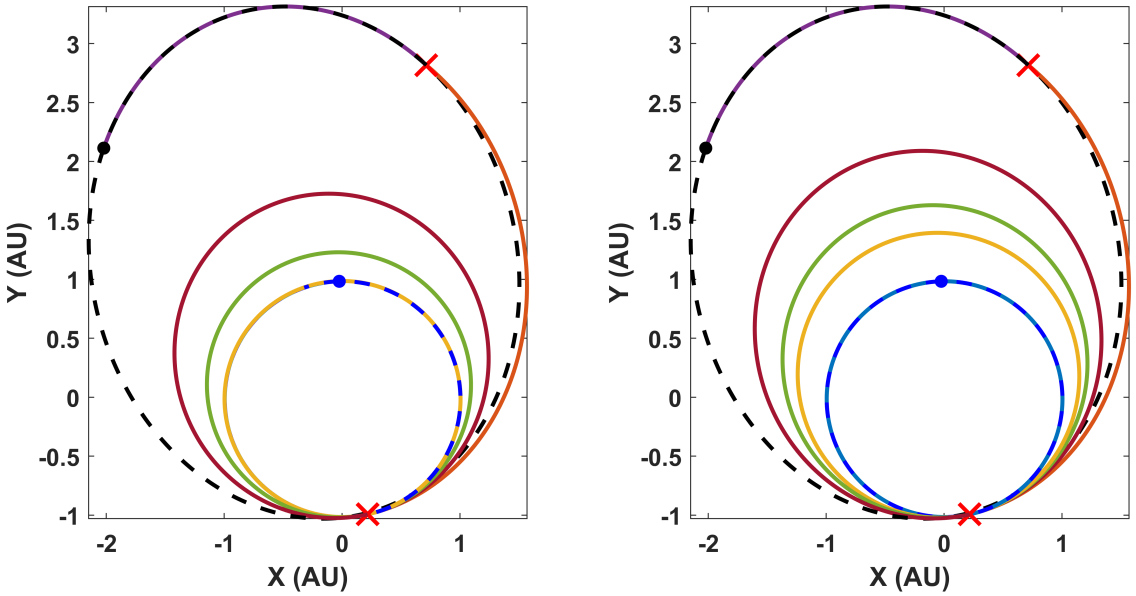

(a) $M = 0, N_1 = 4, N_2 = N_3 = 1$ (b) $M = 2, N_1 = N_2 = N_3 = 1$

Figure 5.9: Five-impulse trajectories with **a**) four, one, and one revolution on phasing orbits; **b**) one, one, and one revolution on phasing orbits and two revolutions on the Earth's orbit. X marker denotes the location of impulses.

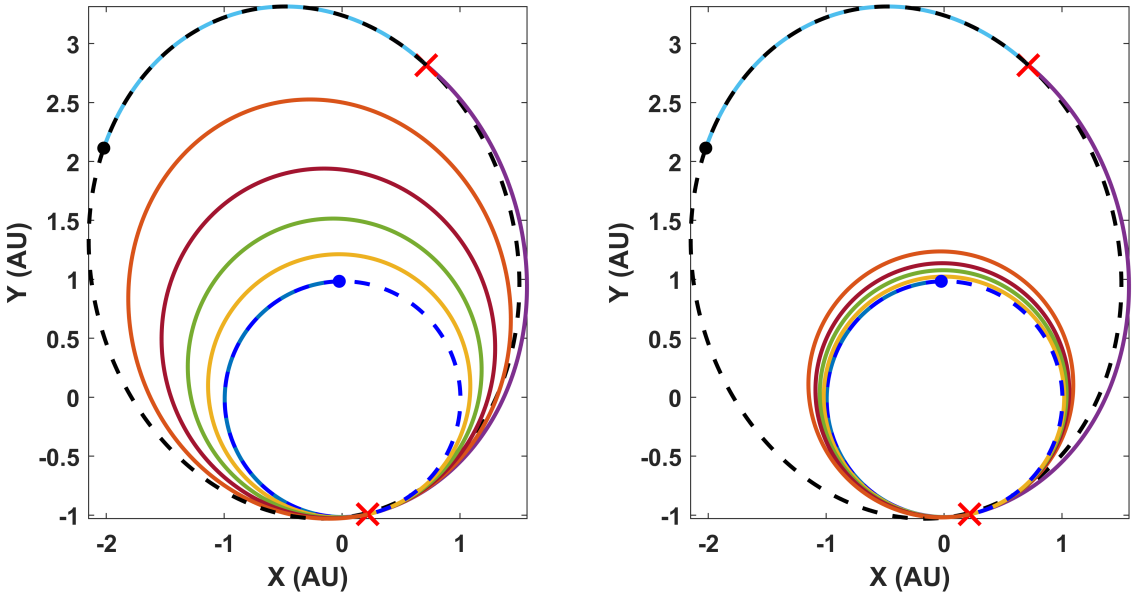

(a) $M = 0, N_1 = N_2 = N_3 = N_4 = 1$ (b) $M = 0, N_1 = N_2 = N_3 = 1, N_4 = 3$

Figure 5.10: Six-impulse trajectories with **a**) one revolution on the four phasing orbits; **b**) one revolution on the first three phasing orbits, and three revolutions on the last phasing orbit. X marker denotes the location of impulses.

total, 7 seven-impulse families are obtained based on feasible combinations of M and N_i (for $i \in \{1, \cdots, 5\}$) values.

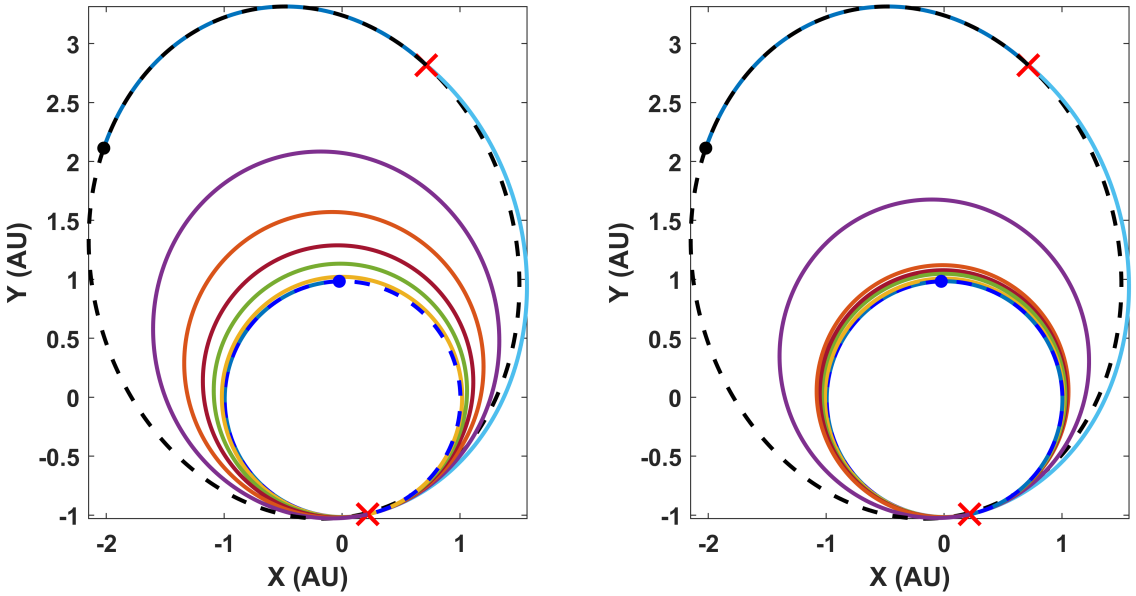

(a) $M = 0, N_1 = N_2 = N_3 = N_4 = N_5 = 1$ (b) $M = 1, N_1 = N_2 = N_3 = N_4 = N_5 = 1$

Figure 5.11: Seven-impulse trajectories with **a**) one revolution on each five phasing orbits; **b**) one revolution on each five phasing orbits and one revolution on the Earth's orbit.X marker denotes the location of impulses.

There is only one eight-impulse solution based on feasible combinations of M and N_i values (for $i \in \{1, \cdots, 6\}$). The eight-impulse family is shown in Fig. 5.12, which has six phasing orbits, each with $N_i = 1$ for $i \in \{1, \cdots, 6\}$. These phasing orbits are shown with yellow, green, red, orange, purple and light blue colors. In summary, the impulsive solutions reported in [4] can be recovered by setting the N values equal to 1 (for the appropriate number of phasing orbits) and M to 0 for the Earth's orbit. Solutions with three and eight impulses are new solutions since only four, five, and six-impulse solutions were reported in [4]. One classification of the solutions is based on the combinations of N and M values for which 134 feasible families have been identified with the same total $\Delta v = 9.907425$ km/s value. Table 5.1 summarizes the total number of multiple-impulse families. We highlight that there are infinitely many iso-Δv solutions and the presented classification is based on the combinations of M, N, N_D, and N_{pf} that result in feasible families of solutions. As a special case, there exists one

unique solution in each solution family for three impulses. Since for this case, one phasing orbit is added to the trajectory and there is one constraint, the solution is obtained uniquely.

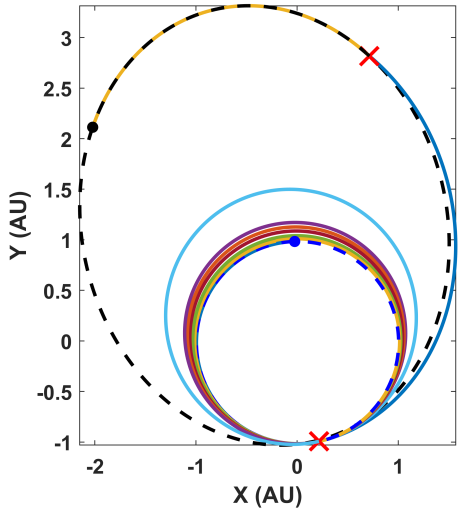

Figure 5.12: The eight-impulse trajectory, where each phasing orbit occurs over one revolution.X marker denotes the location of impulses.

Table 5.1: Classification of impulsive solution families based on the number of impulses obtained from different feasible combinations for M, N_i (for $i \in \{1, \cdots, 6\}$), $N_D \in \{0, 1\}$ and $N_{\text{pf}} \in \{0, 1\}$ values.

Number of Impulses	Number of Solution Families
Three	26
Four	42
Five	37
Six	21
Seven	7
Eight	1

Remark: Due to the enforcement of constraints on the total Δv value, the orbital period value of the phasing orbits should be greater than the orbital period of the Earth and less than the orbital period of the orbit associated with the phase-free two-impulse arc (per Eq. (3.18)). We cannot apply an impulse in the reverse direction of the red $\Delta \boldsymbol{v}$ vector in Fig. 3.3 to place the spacecraft into a phasing orbit with an orbital period less the orbital period of the Earth or the previous phasing orbit. For these cases, the total Δv is always greater than $\Delta v = 9.907425$ km/s.

5.3 GTO to GEO (GTO-GEO) Transfer

To demonstrate that our method is applicable to transfer problems other than the Earth-Dionysus problem, we solve a GTO-GEO transfer problem. The boundary conditions in Cartesian coordinates are given in Table 5.2. Since the GTO and GEO orbits are tangential to each other at the apogee of the GTO, a base solution with a single-impulse ($\Delta v = 1.4873346$ km/s) at the apogee of the GTO is sufficient. We start from the single-impulse base solution and break up the single impulse into smaller impulses without changing the total Δv of the maneuver.

Table 5.2: Cartesian boundary conditions for the GTO-GEO problem.

Parameter	Value
Initial Position (km)	$[6721.95652173912,\ 0,\ 0]$
Initial Velocity (km/s)	$[0,\ 10.0384360619658,\ 1.23256496402036]$
Final Position (km)	$[-42165,\ 0,\ 0]$
Final Velocity (km/s)	$[0,\ -3.07462812005026,\ 0]$
Time of flight (days)	2 (Case 1), 12.011 (Case 2)

The addition of two phasing orbits to the trajectory is shown in Fig. 5.13. This trajectory belongs to the three-impulse family of solutions. Initial and target orbits are shown with blue and black dashed lines, respectively. The blue dot is the departure point and the black dot is the arrival point. Red cross markers represent the impulses. There exists an initial coast, since all impulses are applied at the intersection point of GTO and GEO. Adding two phasing orbits (yellow and green orbits) to the trajectory results in breaking up the total impulse into three smaller impulses. In this case, the mission time is constrained to be 2 days. Therefore, it is not possible to have too many phasing orbits.

Increasing the total time of flight to 12.011 days allows us to introduce more phasing orbits to the trajectory. We add 16 phasing orbits to the trajectory, with one revolution on each of the phasing orbits. The trajectory is shown in Fig. 5.14. The initial and target orbits are identical to the trajectory given in Fig. 5.13. The total Δv is also identical. As the total time of flight increases, the available time to spend on the phasing orbits is longer. Having a larger available time (TOF as shown in Eq. (3.14)) results in having smaller individual impulses to raise the perigee by adding more phasing orbits.

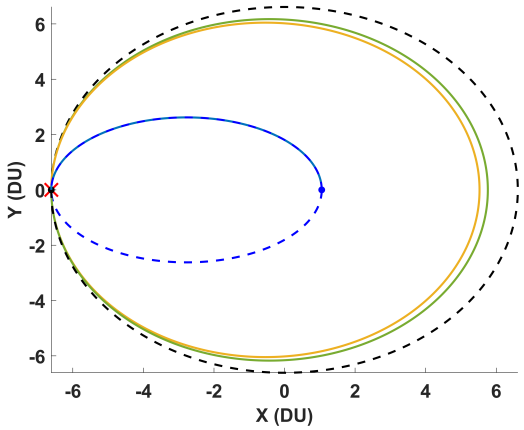

(a) Two-dimensional view of the trajectory.

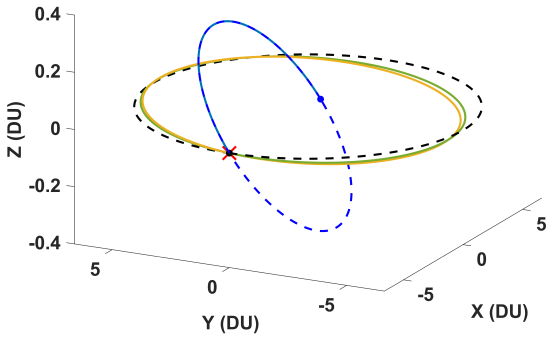

(b) Three-dimensional view of the trajectory.

Figure 5.13: GTO-GEO Case 1: three-impulse minimum-Δv solution. $N_1 = N_2 = 1$. X marker denotes the location of impulses. (1 DU = 6378 km.)

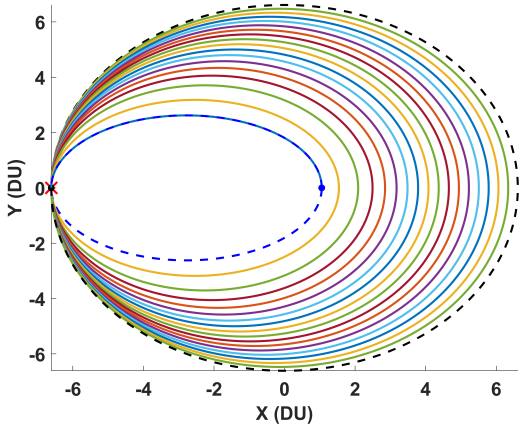

(a) Two-dimensional view of the trajectory.

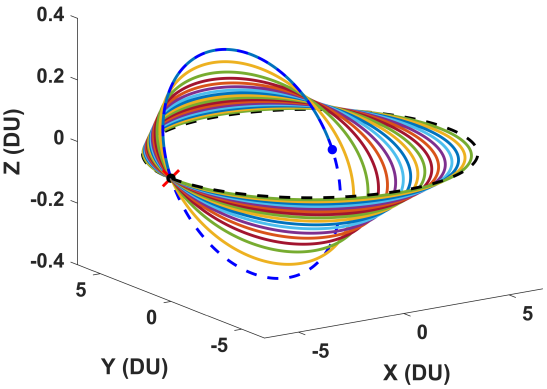

(b) Three-dimensional view of the trajectory.

Figure 5.14: GTO-GEO Case 2: seventeen-impulse minimum-Δv solution ($N_1, \cdots N_{16} = 1$). X marker denotes the location of impulses.

The distribution of the individual impulses in GTO-GEO trajectories is shown in Fig. 5.15. For the three-impulse trajectory, the first impulse has the largest magnitude needed to change the inclination. Since the second orbit is closer to the first one in terms of inclination and semi-major axis, the second and third impulses are relatively smaller. For the seventeen-impulse trajectory, the impulses are more uniformly distributed. The first two impulses are approximately 0.2 km/s, whereas the magnitude of the other impulses decreases uniformly until the last impulse. From an operational point of view, it is possible to increase the time of flight of a mission without affecting the total required impulse; however, we can extend the flight time until the magnitude of the largest impulse falls below the impulse that can be produced by the propulsion system to make the maneuver feasible if individual impulses can not be greater than a maximum limit.

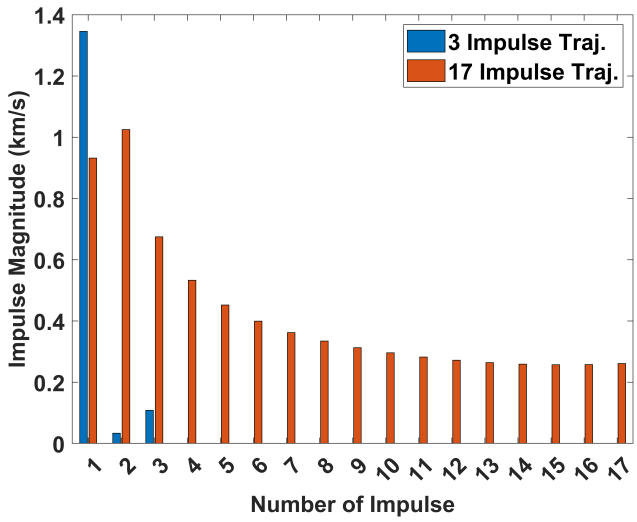

Figure 5.15: Distribution of individual impulses for GTO-GEO trajectories. Magnitudes of the impulses on the 17-impulse trajectory are multiplied by a factor of 5.

5.4 LEO to GEO (LEO-GEO) Transfer

A fixed-time rendezvous maneuver from a circular 300 km altitude Low-Earth Orbit (LEO) to GEO trajectory is generated using the proposed method. The boundaries in Cartesian coordinates are given in Table 5.3, which correspond to a LEO with 28 degrees of inclination. This is a maneuver between non-intersecting orbits with different inclination values. Therefore, we start by solving for the two-impulse base solution as explained in Section 3.1.

Table 5.3: Cartesian boundary conditions for the LEO-GEO problem.

Parameter	Value
Initial Position (km)	$[-6677.99994822088,\ -0.734261017649844,\ -0.390413508385778]$
Initial Velocity (km/s)	$[0.000962087495564221,\ -6.82150753761816,\ -3.62705989590144]$
Final Position (km)	$[42163.9999975184,\ -0.457455672469879,\ 0]$
Final Velocity (km/s)	$[3.33583804464932 \times 10^{-5},\ 3.07466457999987,\ 0]$
Time of flight (days)	1

The two-impulse base solution is plotted in Fig. 5.16. Impulses are shown with red cross markers. Initial and target orbits are shown with dashed blue and black orbits. The time spent on the phase-free arc is 0.220 days and the total Δv is 4.2206849 km/s. The initial and final true anomaly values coincide with the initial and final boundaries of the trajectory given in Table 5.3. This means that there are no late-departure or early-arrival arcs in the solution. Therefore, a remaining time of $TOF = 1 - 0.220 = 0.780$ days is available to be distributed between several phasing orbits. Even though it seems like changing the inclination only at the apogee of the phase-free arc would result in a lower Δv, the minimum-Δv solution distributes inclination change between both maneuvers, which can be proven (see Chp. 6 in Ref. [72]).

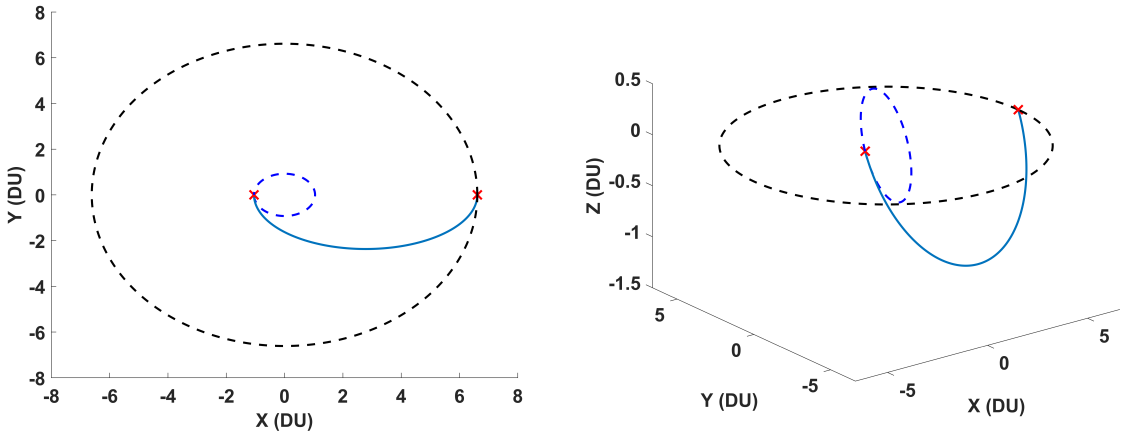

(a) Two-dimensional view of the trajectory.

(b) Three-dimensional view of the trajectory.

Figure 5.16: LEO-GEO two-impulse minimum-Δv solution. X marker denotes the location of impulses.

The trajectory with two phasing orbits is shown in Fig. 5.17. The phase-free arc obtained is shown in red color. The first impulse is the impulse anchor position and it is divided into three impulses. The trajectory has four impulses in total. The apogee of the phasing orbits is

increased gradually. The first impulse to put the spacecraft into the first phasing orbit happens to be the largest impulse in the trajectory and is equal to 1.944 km/s.

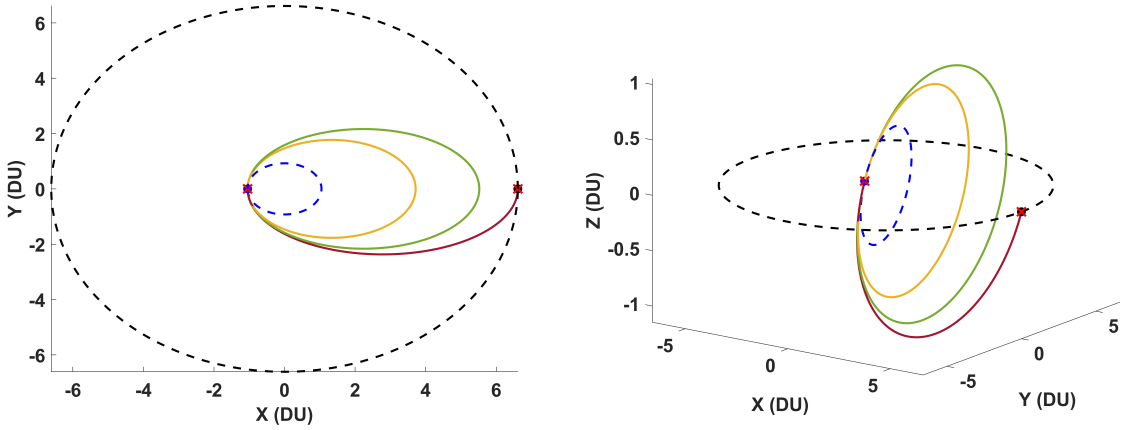

(a) Two-dimensional view of the trajectory

(b) Three-dimensional view of the trajectory

Figure 5.17: LEO-GEO four-impulse minimum-Δv solution. $N_1 = N_2 = 1$. X marker denotes the location of impulses.

5.5 Solution Envelopes for the Family of Solutions

Application of the method explained in Chapter 4 is presented. The constraint on the total TOF determines multiple envelopes of families. Assuming one revolution on each segment results in $TOF = 2490.48$ days. The corners of these envelopes correspond to the extreme cases and define the feasible domain. We plot the solution space and determine the corners of those regions analytically. In this section, we assume that $M = N_D = N_{\text{pf}} = 0$ and $TOF = 2490.48$ days. Our method still applies with non-zero revolutions on any combination of these arcs. In this case, the TOF available for phasing orbits reduces by integer increments of Earth, Dionysus, or transfer orbit (phase-free arc) period. We assume zero revolutions here to highlight the versatility of the method with the widest range of orbital periods for phasing orbits.

Phasing orbit periods are plotted with respect to the first phasing orbit period, T_1. Phasing orbit periods are functions of the α parameters. When $\alpha = 0$, $T(\alpha) = 365.25$ days, which is the orbital period of the Earth (the orbit from which the spacecraft departs). When $\alpha = 1$, $T(\alpha) = 1161.47$ days, which is the orbital period associated with the phase-free arc. These two

orbital period values are the bounds on the orbital periods of phasing orbits. Another constraint on the orbital periods is $T_1 \leq T_2 \leq \cdots \leq T_{n_p}$ since the α parameters have the constraints defined in Eq. (3.16). However, we relax the constraints on the orbital periods by including equality conditions to analyze the extreme points in the solution space by allowing α values to be equal.

In Fig. 5.18a, the relation between orbital periods of the first and second phasing orbits is shown. As the orbital period of the first phasing orbit increase, the second orbital period decreases. We can analytically determine the relation between T_1 and T_2. The minimum value of T_1 is $T_{1,\text{min}} = 365.25$ days. From the total TOF constraint (i.e., Eq. 3.14), $T_{2,\text{max}} = (TOF - N_1 T_{1,\text{min}})/N_2 = 1062.61$ days. The maximum value of T_1 is when $T_{1,\text{max}} = T_{2,\text{min}} = TOF/(N_1 + N_2) = 830.16$ days.

Five-impulse solution envelopes are shown in Fig. 5.18b. In Fig. 5.18b, orbital periods for the second (T_2) and third (T_3) phasing orbits create polygonal regions in green and gray color. Infinitely many feasible solutions lie inside these polygonal regions. The region is bounded below with the value of T_1 which is shown with the blue line.

The corners of these regions can be analytically determined. Leftmost corners (corners '1', '2', '3' in Fig. 5.18b) for both regions are when $T_{1,\text{min}} = 365.25$ days, which is the lowest value for $\alpha = 0$. Using Eq. (3.16), and considering the $T_2 \leq T_3$ constraint, the minimum value of T_3 is the maximum value of T_2 corresponding to corner '2',

$$\begin{aligned} T_2 + T_3 &= TOF - T_{1,\text{min}}, \\ T_{2,\text{max}} = T_{3,\text{min}} &= (TOF - T_{1,\text{min}})/2 = 1062.62 \text{ days}. \end{aligned} \tag{5.1}$$

The values of $T_{3,\text{max}}$ (corner '3') and $T_{2,\text{min}}$ (corner '1') are calculated as,

$$T_{3,\text{max}} = T(\alpha = 0) = 1161.47 \text{ days}, \tag{5.2}$$

$$T_{2,\text{min}} = TOF - T_{1,\text{min}} - T_{3,\text{max}} = 963.77 \text{ days}. \tag{5.3}$$

Thus, we were able to calculate the leftmost corners (corners '1', '2', '3') of solution regions for T_2 and T_3. Additionally, $T_{3,\text{max}}$ being the maximum orbital period value, creates

another corner (corner '4' in Fig. 5.18b) on the solution region of T_3, which affects the T_2 region too. The lower limit of T_2 becomes equal to T_1 after this corner point '4'. Therefore, at this corner point $T_1 = T_2$ while $T_{3,\text{max}}$. Using Eq. (3.16),

$$T_{1,\text{corner}} = T_{2,\text{corner}} = (TOF - T_{3,\text{max}})/2 = 664.51 \text{ days}. \tag{5.4}$$

The remaining corner is, corner '5' in Fig. 5.18b, where all the regions converge to the right-most point, which is obtained as $T_1 = T_2 = T_3 = TOF/3 = 830.16$ days. This extreme solution at which the orbital period of all phasing orbits is equal for $n_p = 3$ is equivalent to the case with $n_p = 1$ and $N_1 = 3$. Therefore, we were able to identify the corner points of these regions by utilizing the constraints of the problem. This approach can also be applied to cases with more intermediate phasing orbits. The relations to obtain the corners of solution regions can be generalized to cases with more intermediate phasing orbits as explained in Chapter 4.

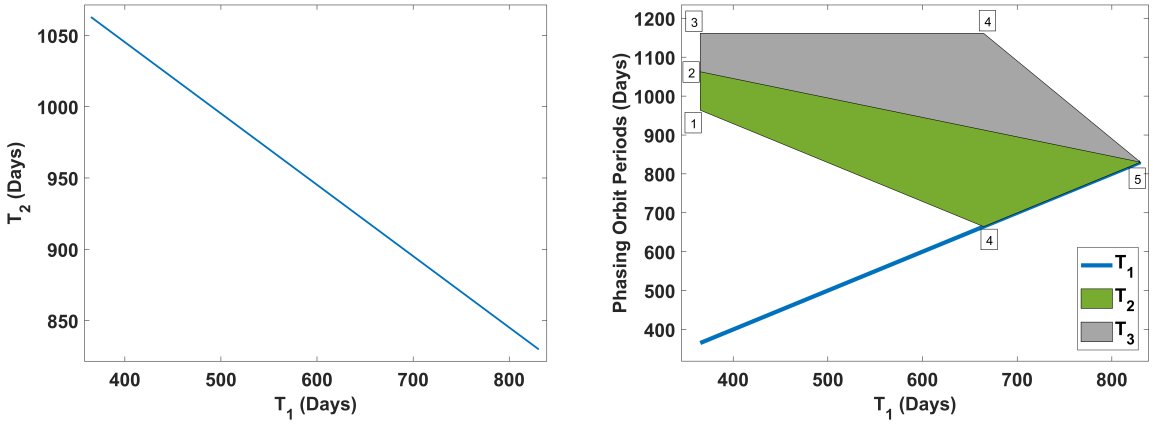

(a) $N_1 = 1, N_2 = 2$ (b) $N_1 = N_2 = N_3 = 1$

Figure 5.18: Phasing orbit periods for **a**) Four-impulse solutions; **b**) Five-impulse solutions.

The solution regions are shown for the six-impulse case in Fig. 5.19 in both two- and three-dimensional views. The polygonal region for T_2 is the green region and shares a common line with the gray region which is for T_4 at the upper line of the green triangular region and the lower line of the green polygonal region. The yellow region is for T_3 and it is on top of the other two regions. This means that at the intersection of yellow and green, there exist solutions when T_2 and T_3 are equal. On the intersection of the gray and yellow region, solutions exist where T_2 and

T_3 are equal. All the regions share one common line, where $T_2 = T_3 = T_4 = (TOF - T_1)/3$ for $T_1 \in [T_E, TOF/4]$ which is shown with the red colored line in Fig. 5.19a. The upper limit of the T_4 region is on the boundary ($T(\alpha = 1)$) for a finite interval up until $T_1 = T_2 = 443.00$ days.

The solution regions for the seven-impulse case are shown in Fig. 5.20 in both two- and three-dimensional views. The T_5 upper bound is not equal to the upper bound constraint. Therefore, all orbital period solution regions are triangular. The corners correspond to when all orbital periods are equal to each other, and the minimum and maximum range of solutions are when $T_{1,\text{min}} = T_E$. Similar to the six-impulse case, the intersection of all the solution regions corresponds to $T_2 = T_3 = T_4 = T_5 = (TOF - T_1)/4$ where $T_1 \in [T_E, TOF/5]$ as shown in Fig. 5.20a with the red line. Determining the envelopes of solutions is useful for feasibility analysis to see the ranges and intersections of the solutions.

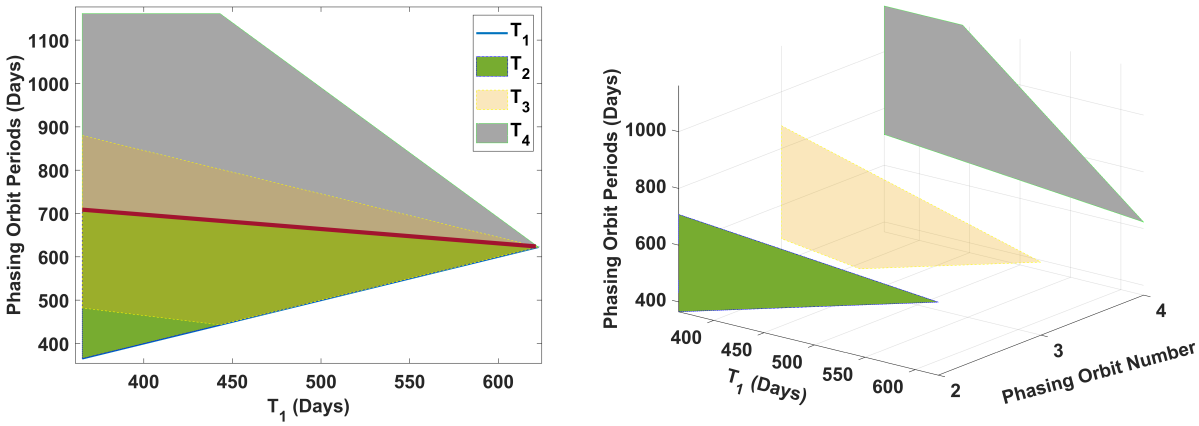

(a) $N_1 = N_2 = N_3 = 1$ (b) $N_1 = N_2 = N_3 = 1$

Figure 5.19: Phasing orbit periods for a six-impulse family **a**) two-dimensional view; **b**) three-dimensional view.

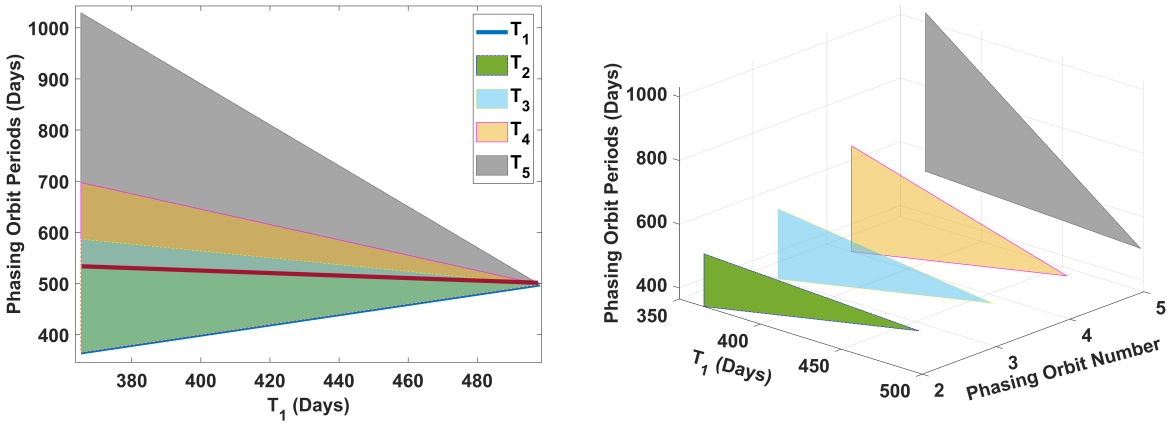

(a) $N_1 = N_2 = N_3 = N_4 = 1$ (b) $N_1 = N_2 = N_3 = N_4 = 1$

Figure 5.20: Phasing orbit periods for a seven-impulse family **a**) two-dimensional view; **b**) three-dimensional view.

Chapter 6

Lower and Upper Bounds on the Number of Impulses

The existence of infinitely many optimal iso-Δv trajectories is a major finding in our quest to answer the transfer maneuver Edelbaum considered in his seminal 1967 paper [2]. In particular, the results actually allow us to provide analytic bounds on the lower (required) and upper (allowable) number of impulses for three important classes of long-time-horizon, minimum-Δv maneuvers in an inverse-square gravity model:

1. fixed-time-of-flight, rendezvous between two bodies (i.e., time-dependent states corresponding to the two bodies on two different arbitrary orbits),

2. free-terminal-time, rendezvous, but the maneuver is between any two points on two different arbitrary orbits,

3. free-terminal-time, transfer.

The second and third classes and their solutions for multiple-revolution maneuvers have remained elusive for more than five decades. We have expanded the range of the possible number of impulses for the benchmark Earth-Dionysus problem. In particular, we have shown that the three- to eight-impulse family of solutions exist with the same known total optimal Δv value. In fact, the solutions that we have obtained correspond to the first class of maneuvers. For the same optimal Δv value, the number of impulses can vary from the least three impulses to a maximum of eight impulses. The key unknown in this step is to consider the lower bound of Eq. (3.18). For the Earth-Dionysus problem, $T(\alpha = 0)$ is 365.25 days and TOF is 2490.48 days, giving $365.25 < \frac{2490.48}{n_p}$, or $n_p < 6.82$ giving a maximum of 6 phasing orbits and 8

impulses. Analysis of the time constraint leads to $1 \leq n_p \leq 6$. This is a remarkable result in the sense of providing analytic relations for determining bounds on the minimum (required) and maximum (allowable) number of impulses needed for fixed-time rendezvous maneuvers. It is also applicable to any large, but finite-time-horizon maneuver.

The second class is an extension of the first class but can be connected to the third class. In other words, while the original Earth-Dionysus problem has been formulated as a fixed-time-of-flight, minimum-Δv rendezvous between two fixed points on two different orbits, the free-terminal-time transfer problem between two orbits is embedded in the family of extremal solutions due to the presence of late-departure and early-arrival arcs that appear in impulsive trajectories [4]. The solutions consist of a departure point on an initial 6-D manifold to an entry point on a different 6-D manifold. Moreover, while there is definitely a lower bound on the time of flight associated with the minimum-Δv transfer maneuver between the two manifolds (i.e., the time of flight associated with the phase-free two-impulse arc shown in Fig. 5.5a), it can be concluded that no upper bound can be defined for the time of flight as long as there is sufficient time for the spacecraft to spend on the four major phases. This can be achieved, for instance, by adding integer multiples of the Earth's orbital period to the current available phasing time (i.e., $TOF = 2490.48 + \kappa T_E$ days and $\kappa \in \mathbb{N}$).

For free-final-time, rendezvous problems, we should also account for the total time by adding multiples of the orbital periods of the target, e.g., $\beta \times T_D$, where T_D is the orbital period of asteroid Dionysus and $\beta \in \mathbb{N}$. While the total time of flight can be increased, it is always possible to consider larger M and N_i values (see Eq. (3.14)) for a number of phasing orbits. As the TOF value increases, the possibilities for introducing more phasing orbits grow, and one can obtain multiple-impulse solutions with the same total minimum-Δv value. For the Earth-Dionysus problem, the minimum number of impulses for a phase-free transfer is two, whereas the minimum number of impulses is three for a phase-constrained version of the problem. The universal feature of all multi-impulse minimum-Δv solutions, however, is that they require the same total Δv value.

In general, if we consider a free-final-time transfer maneuver between two orbits, the upper number of impulses has no limit if we are allowed to add as much time possible for phasing

maneuvers per our discussion while the lower number of impulses is two for the free-final-time transfer problem. Note that time being unbounded does not cause an ambiguity, since the total optimal Δv remains the same. However, if the time of flight is large but finite, it is *always* possible to determine the maximum (allowed) number of impulses.

In terms of the mathematical formulation of these different maneuver cases, we can also revisit Eq. (3.1) to generate phase-free maneuvers on free-time transfers. If we consider free-time rendezvous, then the t_{pf} becomes a function of the initial and final true anomaly, which potentially increases the total Δv obtained in the free-time transfer problem. However, the addition of phasing orbits provides an additional degree of freedom to the problem so that the minimum Δv can be recovered. In the proposed formulation, this phasing time parameter (TOF in the constraint equation Eq. (3.14)) should be between the orbital period of the initial and target orbits. Since it is a free-time rendezvous problem, the total time of flight can be increased by adding multiples of the target orbit orbital period to increase flexibility to break up the total impulse and add more phasing orbits. For the fixed-time rendezvous problem, the initial and final true anomaly and t_{pf} are fixed. If these were the only design parameters, then the solution could be obtained by solving Lambert's problem, resulting in a higher total Δv. However, with the proposed method, phasing orbits and coast arcs can be introduced to the trajectory to achieve minimum-Δv.

Alternatively, every different maneuver case can be obtained first by solving the phase-free two-impulse arc without altering Eq. (3.1). The current formulation generates the free-time transfer solution. If the free-time rendezvous maneuver is considered, then adding phasing orbit and increasing the total mission time can generate the minimum-Δv solution by following the steps explained in Section 3.4. The available time (TOF) should be larger than the orbital period of the initial orbit for the proposed method. For fixed-time rendezvous problems, coast arcs and/or phasing orbits can be introduced to generate the trajectory with the minimum-Δv using the proposed method, if the available time (TOF) is longer than the orbital period of the initial orbit. In other words, this method can be used for time-feasibility studies of minimum-Δv maneuvers and allows to recover minimum-Δv for each maneuver type. This process is explained in Fig. 6.1. In Fig. 6.1, the green arc represents the phase-free arc obtained

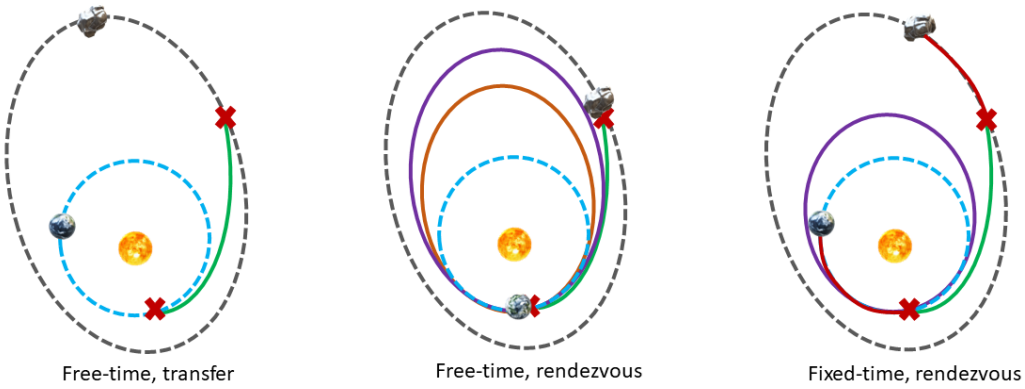

Figure 6.1: Three different maneuver types to obtain minimum-Δv solution.

from solving a phase-free problem which is shown as a free-time transfer maneuver. Then, a number of phasing orbits are added to the free-time rendezvous maneuver in the middle example trajectory. Finally, coast arcs and phasing orbits are added to the trajectory for fixed-time rendezvous at the left-most trajectory in Fig. 6.1.

The benefit of free-time transfer is that it generates the minimum-Δv maneuver regardless of flight time and phasing. Thus, it is the most general solution. Free-time rendezvous is a step for incorporating the phasing to match the target body. Fixed-time rendezvous is the most constrained case but it can match the minimum possible Δv from free-time transfer with the addition of phasing orbits and coast arcs. They provide simpler problems to bound the solution space of the more complex problems.

Chapter 7

Generation and Interpretation of the Primer Vector for Trajectories with Phasing Orbits

Necessary conditions for optimal impulsive trajectories were derived by Lawden in his seminal work [5] in terms of the primer vector norm and its derivative. The primer vector defines the optimal direction of the impulse vector. The details about the primer vector theory are explained in Chapter 2.4. In order to evaluate the time history of the primer vector, Φ_2^{-1} has to exist to solve for the initial value of the primer vector derivative in Eq. (2.17).

For a general phasing orbit, only the velocity magnitude is constrained, and the velocity direction is free (assuming a direction is not considered). This additional degree of freedom on phasing orbits results in singularities on Φ_2. One revolution on a phasing orbit results in an identity STM where Φ_2^{-1} does not exist. In such cases, the primer vector time history cannot be determined by using Eq. (2.17). However, Lawden's necessary conditions for optimality can be utilized to overcome this issue. Since it is known that these solutions are extremal, we can use the fact that the primer vector derivative is continuous, and that the primer vector and its derivative are orthogonal at the impulse instances. Thus, the initial value of the primer vector derivative is simply its value at the next impulse point, since it is continuous. In the cases that we have considered, the primer vector is also known, since the $\Delta \boldsymbol{v}$ is known at the impulse points of the fundamental phase-free two-impulse arc (see Chapter 3). Therefore, time histories can be obtained by propagating the primer vector and its derivative backward for the time of flight spent on all phasing orbits. However, if the spacecraft remains on the phasing orbit and makes multiple revolutions (as has been the case for many of the solutions that we have presented) one has to consider a new interpretation of the primer vector time history.

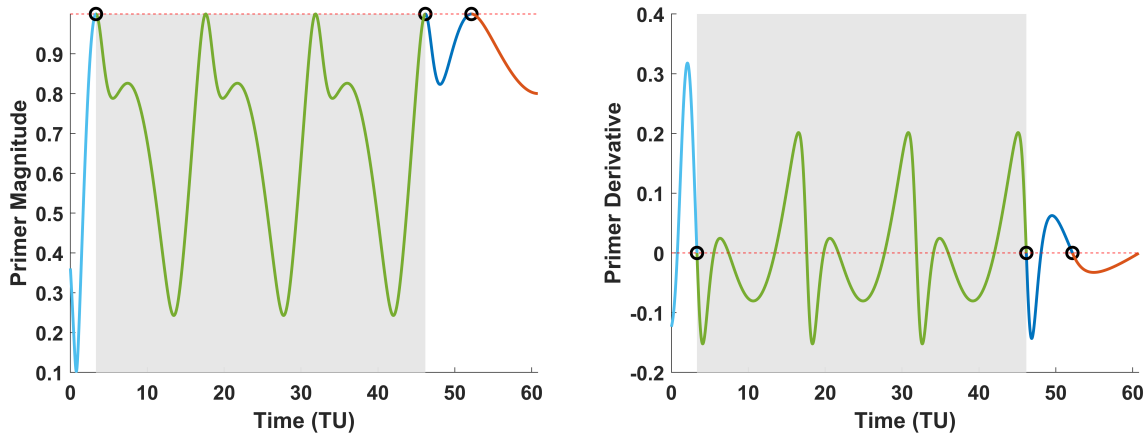

(a) (b)

Figure 7.1: **a**) Primer vector magnitude vs. time when one phasing orbit is added to the trajectory. **b**) $\dot{p}$ vs. time with one phasing orbit with three revolutions around the Sun.

An example of primer magnitude and primer derivative is given in Fig. 7.1 where circles indicate the impulses. Note that the derivative refers to the derivative of the norm given in Eq. (2.14). These plots are for the solution given in Fig. 5.7a. In this solution, the spacecraft makes three revolutions on the phasing orbit. This multi-revolution solution is apparent in the primer vector magnitude time history plotted in Fig. 7.1a as the primer norm cycles with the same profile in the shaded region.The green curve has three cycles as it returns to the impulse anchor position and it is possible to have an impulse. As we discussed in Section 3.2, applying any impulse in a different location would increase the total Δv. The shaded region represents the time interval where the spacecraft is in the phasing orbit. It can be seen that after the impulse at the beginning of the shaded area, there exist three impulse opportunities as the primer magnitude becomes unity. Thus, on phasing orbits, we are dealing with a new notion, i.e., *potential impulse opportunity*. However, only at the last impulse opportunity (on the phasing orbit), an impulse happens. At these potential impulse opportunities, the derivative of the norm of the primer vector is equal to zero (shown in Fig. 7.1b) which also indicates that all the potential impulse opportunities satisfy the necessary conditions of optimality. Here, it is instructive to note that the $n_p = 1$ and $N_1 = 3$ family depicted in Fig. 7.1b lies on the bifurcation point of the family with $n_p = 3$ and $T_1 = T_2 = T_3$.

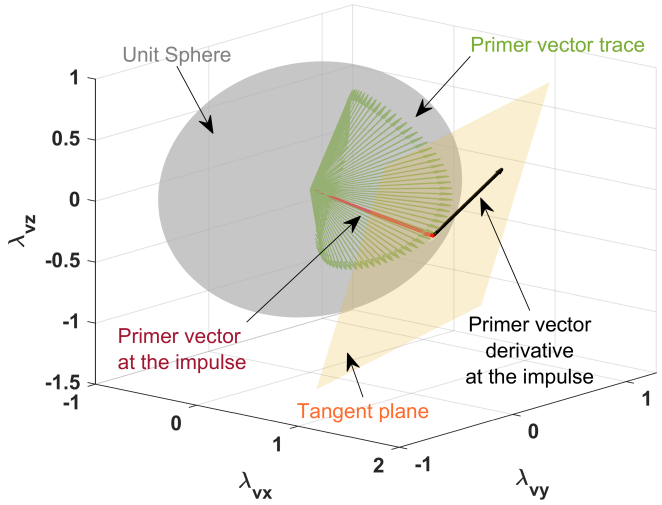

Figure 7.2: Evolution of the primer vector (green) and primer vector derivative (black) on the phasing orbit, shown as a gray region in Fig. 7.1.

To show the evaluation of the primer vector with time on the phasing orbits, the primer vector and primer vector derivative are plotted in a three-dimensional plot in Fig. 7.2. Primer vectors are plotted with green vectors. When there exists an impulse opportunity, the primer vector norm becomes unity. This is shown with the red arrow. The derivative of the primer vector, when its magnitude becomes one, is shown with a black arrow that lies on the supporting plane tangent to the sphere defined by the $||\mathbf{p}|| = 1$ constraint. Any impulse corresponds to a point on the surface of the primer vector sphere. However, the derivative of the primer vector will lie on the supporting hyperplane. In this case, when we are analyzing the impulses at the impulse anchor position, we will have a unique supporting plane. Whenever there is a potential impulse opportunity, the primer vector and its derivative are orthogonal and shown with the red and black colored vectors, respectively. All the shown green vectors correspond to the primer vector in between the impulses on the phasing orbit, which means that these vectors lie interior to the unit sphere since the magnitude of the primer vector is less than the unity in between the impulses on any extremal solution. The tip of the green vectors denotes the locus traced by the primer vectors on one of the phasing orbits. The evolution of the primer vectors will be different on different phasing orbits. Still, the same interpretation applies and the location of the intermediate impulses will be the same on the sphere.

Chapter 8

Concluding Remarks

Generating fuel-optimal trajectories is critical to utilize the limited sources of a spacecraft for space exploration. The previous investigations on the Earth-Dionysus problem showed that there exist trajectories with the exact same impulse magnitude. This thesis explained how those solutions can be obtained and showed that there exist infinitely many such solutions. The results are generalized to solve different impulsive trajectories. This work performed in this thesis contributes to the development of an analytic method to generate iso-impulse trajectories with multiple phasing orbits. These iso-impulse trajectories are generated starting from a base two-impulse trajectory. Additionally, the study investigates the upper and lower bounds on the number of impulses. This research effort aims to propose a fast approach for maneuver placement for impulsive trajectory generation.

In order to review the main findings of this research effort, the proposed questions in the introduction section are answered.

1. *How these iso-impulse solutions can be generated for long-time-horizon multiple-revolution impulsive trajectories?*

   Investigations of different solutions to the Earth-Dionysus problem showed that the impulses are located at two distinct points. From this observation, a phase-free two-impulse minimum-Δv optimization problem is formulated. In order to satisfy the rendezvous problem and the fixed total time of flight of the mission, multiple phasing orbits are added to the trajectory by breaking up the first impulse at the impulse anchor position. The direction of the impulse is kept constant, since changing the direction increases the

total Δv. Therefore, only the magnitude of the impulse is varied without exceeding the amount of total impulse magnitude. The resulting problem is expressed with a constraint equation including the number of revolutions and the orbital period of phasing orbits. It is shown that orbital period information can be calculated once the impulse amount is known or vice versa. Therefore, the number of unknowns is increased as the number of phasing orbits is added to the trajectory. For the three-impulse case where there is one phasing orbit in the trajectory, the solutions obtained are unique since the number of constraints is equal to the number of unknowns. For the cases when the number of impulses is four or more than four, the number of unknowns is higher than the number of constraints. This resulted in having infinitely-many iso-impulse solutions.

For the Earth-to-Dionysus problem, 134 feasible families are obtained, based on the combinations of motions on the four phases for one impulse anchor position. The family of impulsive solutions spans a minimum of three and a maximum of eight impulses for solutions with the same total impulse value. We have obtained 130 new impulsive families based on the combinations of the four aforementioned phases.

The applicability of the proposed method on different impulsive trajectory optimization problems is demonstrated by solving GTO-GEO and LEO-GEO problems. Results show that there exists a family of solutions for each case. In addition, for problems with phasing orbits, the primer vector can be reconstructed using the continuity of the primer vector and its derivative at the boundary of the phasing orbits. However, when a spacecraft enters a phasing orbit and makes multiple revolutions, there are a number of "potential impulse opportunities" all of which satisfy Lawden's necessary conditions of optimality, but no impulse is applied at the potential impulse opportunities except for time instants at the entry to and exit from a phasing orbit.

2. *How can we classify iso-impulse solutions and what is the solution space for this family of solutions?*

   In order to classify the iso-impulse solutions, different number of revolutions on different segments of the trajectory is considered. The solutions are classified by the number

of revolutions on these main segments: the initial orbit or Earth's orbit, the number of phasing orbits, a phase-free arc, the target orbit, or Dionysus' orbit. It is concluded that as the number of revolutions increased on different segments of the trajectory, it decreases the possibility of having more revolutions on the rest of the segments due to having a fixed time problem.

To determine the solution spaces of infinitely-many iso-impulse solutions, the extreme cases in the family of solutions are investigated. Some of these extreme cases are defined as when the first phasing orbit is at its minimum when all the phasing orbit periods are equal to each other when the last phasing orbit is at its maximum value. These extreme cases are used to derive analytical relations to generate solution envelopes. It is concluded that the first phasing orbit orbital period bounds the solution space from below. The solution orbital period lies in between the initial and last phasing orbit orbital period. All the solution envelopes converge or bifurcate from the point where all orbital periods are equal to each other.

3. *Can the infinitely many solutions be used to determine the upper and lower number of impulses for long-time-horizon multiple-revolution trajectories?*

   In order to determine the lower and upper bounds of the impulses, an analytical relation is derived. This relation includes the lower and upper bound of the orbital periods when the first impulse placing spacecraft into the phasing orbit is zero and the case where the total impulse is not distributed but applied at once. It is known that the total time of flight spent on the phasing orbits is constant. If there exists a solution when all of the orbital periods of phasing orbits are equal to each other, then one can conclude that there exist infinitely many solutions for that particular family. When the number of phasing orbits added to the trajectory is unknown, the inequality relation can be utilized to determine the range of the number of impulses.

   The analysis is extended to free-terminal-time rendezvous maneuvers and free-terminal-time transfer-type maneuvers. It is discussed that the free final time rendezvous maneuver's upper number of impulses is infinity since the total time of the mission can be

increased and more and more phasing orbits can be added to the trajectory. The lower bound of the number of impulses can be a two or a three-impulse maneuver. For free final-time transfer maneuvers, there exists a lower bound on the time for the connecting arc. Therefore, the lower bound can be a two-impulse trajectory, but the upper limit is infinity since the total mission time can be increased and more phasing orbits can be added to the trajectory.

References

[1] Conway, B., *Spacecraft Trajectory Optimization*, Vol. 29, Cambridge University Press, 2010.

[2] Edelbaum, T., "How many impulses?" *3rd and 4th Aerospace Sciences Meeting*, American Institute of Aeronautics and Astronautics, New York,NY,U.S.A., Jan. 1966.

[3] Walsh, M. T. and Peck, M. A., "Survey of Methods for Calculating Impulsive ΔV-Minimizing Orbit Transfer Maneuvers," *AIAA Scitech 2020 Forum*, American Institute of Aeronautics and Astronautics, Orlando, FL, Jan. 2020.

[4] Taheri, E. and Junkins, J. L., "How Many Impulses Redux," *The Journal of the Astronautical Sciences*, Vol. 67, No. 2, June 2020, pp. 257–334.

[5] Lawden, D. F., *Optimal trajectories for space navigation*, Vol. 3, Butterworths, 1963.

[6] Lion, P. M. and Handelsman, M., "Primer Vector on Fixed-Time Impulsive Trajectories." *AIAA Journal*, Vol. 6, No. 1, Jan. 1968, pp. 127–132.

[7] Jezewski, D. J. and Rozendaal, H. L., "An efficient method for calculating optimal free-space n-impulse trajectories." *AIAA Journal*, Vol. 6, No. 11, Nov. 1968, pp. 2160–2165.

[8] Prussing, J. E., "Illustration of the primer vector in time- fixed, orbit transfer." *AIAA Journal*, Vol. 7, No. 6, June 1969, pp. 1167–1168.

[9] Carter, T., "Optimal impulsive space trajectories based on linear equations," *Journal of optimization theory and applications*, Vol. 70, No. 2, 1991, pp. 277–297.

[10] Stern, R. G. and Potter, J. E., "Optimization of Midcourse Velocity Corrections," *IFAC Proceedings Volumes*, Vol. 2, No. 1, June 1965, pp. 70–83.

[11] Arzelier, D., Kara-Zaitri, M., Louembet, C., and Delibasi, A., "Using Polynomial Optimization to Solve the Fuel-Optimal Linear Impulsive Rendezvous Problem," *Journal of Guidance, Control, and Dynamics*, Vol. 34, No. 5, Sept. 2011, pp. 1567–1576.

[12] Fossà, A. and Bettanini, C., "Optimal rendezvous trajectory between Sample Return Orbiter and Orbiting Sample Container in a Mars Sample Return mission," *Acta Astronautica*, Vol. 171, June 2020, pp. 31–41.

[13] Huang, A.-Y., Luo, Y.-Z., and Li, H.-N., "Fast Estimation of Perturbed Impulsive Rendezvous via Semi-Analytical Equality-Constrained Optimization," *Journal of Guidance, Control, and Dynamics*, Vol. 43, No. 12, Dec. 2020, pp. 2383–2390.

[14] Kim, Y. and Park, S.-Y., "Nonsingular Dual–Primal Algorithm for Fuel-Optimal Impulsive Rendezvous," *Journal of Guidance, Control, and Dynamics*, Vol. 42, No. 4, April 2019, pp. 737–751.

[15] Prussing, J. E., "Optimal Two- and Three-Impulse Fixed-Time Rendezvous in the Vicinity of a Circular Orbit," *Journal of Spacecraft and Rockets*, Vol. 40, No. 6, Nov. 2003, pp. 952–959.

[16] Gobetz, F. W. and Doll, J. R., "A survey of impulsive trajectories." *AIAA Journal*, Vol. 7, No. 5, May 1969, pp. 801–834.

[17] Wen, C., Zhao, Y., and Shi, P., "Precise Determination of Reachable Domain for Spacecraft with Single Impulse," *Journal of Guidance, Control, and Dynamics*, Vol. 37, No. 6, Nov. 2014, pp. 1767–1779.

[18] Chen, Q., Qiao, D., Shang, H., and Liu, X., "A new method for solving reachable domain of spacecraft with a single impulse," *Acta Astronautica*, Vol. 145, 2018, pp. 153–164.

[19] Zhang, G., Cao, X., and Ma, G., "Reachable domain of spacecraft with a single tangent impulse considering trajectory safety," *Acta Astronautica*, Vol. 91, 2013, pp. 228–236.

[20] Hohmann, W., *The attainability of heavenly bodies*, No. 44, National Aeronautics and Space Administration, 1960.

[21] Barrar, R., "An analytic proof that the Hohmann-type transfer is the true minimum two-impulse transfer," Tech. rep., System Development Corp Santa Monica, California, 1962.

[22] Edelbaum, T., "Some extensions of the Hohmann transfer maneuver," 1959.

[23] Hoelker, R. F. and Silber, R., "The bi-elliptical transfer between co-planar circular orbits," *Planetary and Space Science*, Vol. 7, 1961, pp. 164–175.

[24] Carter, T. and Humi, M., "Two-impulse, bi-parabolic, and bi-elliptical transfers between coplanar elliptical orbits," *Acta Astronautica*, Vol. 177, Dec. 2020, pp. 158–171.

[25] Prussing, J. E. and Chiu, J.-H., "Optimal multiple-impulse time-fixed rendezvous between circular orbits," *Journal of Guidance, Control, and Dynamics*, Vol. 9, No. 1, Jan. 1986, pp. 17–22.

[26] Broucke, R. A. and Prado, A. F. B. A., "Orbital planar maneuvers using two and three-four (through infinity) impulses," *Journal of Guidance, Control, and Dynamics*, Vol. 19, No. 2, March 1996, pp. 274–282.

[27] Caruso, A., Quarta, A. A., and Mengali, G., "Optimal transfer between elliptic orbits with three tangential impulses," *Advances in Space Research*, Vol. 64, No. 4, Aug. 2019, pp. 861–873.

[28] Lawden, D. F., "Optimal transfers between coplanar elliptical orbits," *Journal of Guidance, Control, and Dynamics*, Vol. 15, No. 3, May 1992, pp. 788–791.

[29] Small, H. W., "Minimum N-impulse time-free transfer between elliptic orbits," *AIAA Journal*, Vol. 9, No. 4, April 1971, pp. 594–599.

[30] Prussing, J. E., "Optimal two- and three-impulse fixed-time rendezvous in the vicinityof a circular orbit," *AIAA Journal*, Vol. 8, No. 7, July 1970, pp. 1221–1228.

[31] Shen, H.-X., Casalino, L., and Luo, Y.-Z., "Global Search Capabilities of Indirect Methods for Impulsive Transfers," *The Journal of the Astronautical Sciences*, Vol. 62, No. 3, Sept. 2015, pp. 212–232.

[32] Hughes, S. P., Mailhe, L. M., and Guzman, J. J., "A comparison of trajectory optimization methods for the impulsive minimum fuel rendezvous problem," *26th Annual Guidance and Control Conference*, 2003.

[33] Serra, R., Arzelier, D., and Rondepierre, A., "Analytical Solutions for Impulsive Elliptic Out-of-Plane Rendezvous Problem via Primer Vector Theory," *IEEE Transactions on Control Systems Technology*, Vol. 26, No. 1, Jan. 2018, pp. 207–221, Conference Name: IEEE Transactions on Control Systems Technology.

[34] Sandrik, S., *Primer-Optimized Results and Trends for Circular Phasing and Other Circle-to-Circle Impulsive Coplanar Rendezvous*, Ph.D. thesis.

[35] Bell, J. L., *Primer vector theory in the design of optimal transfers involving libration point orbits*, Ph.D., Purdue University, United States, Indiana, ISBN: 9798209118084.

[36] Bokelmann, K. A. and Russell, R. P., "Optimization of Impulsive Europa Capture Trajectories using Primer Vector Theory," *The Journal of the Astronautical Sciences*, Vol. 67, No. 2, June 2020, pp. 485–510.

[37] Olympio, J. T. and Izzo, D., "Designing optimal multi-gravity-assist trajectories with free number of impulses," *International Symposium on Space Flights Dynamics, Toulouse, France. ESA ESTEC*, 2009.

[38] Arzelier, D., Louembet, C., Rondepierre, A., and Kara-Zaitri, M., "A new mixed iterative algorithm to solve the fuel-optimal linear impulsive rendezvous problem," *Journal of Optimization Theory and Applications*, Vol. 159, No. 1, 2013, pp. 210–230.

[39] Abdelkhalik, O. and Mortari, D., "N-impulse orbit transfer using genetic algorithms," *Journal of Spacecraft and Rockets*, Vol. 44, No. 2, 2007, pp. 456–460.

[40] Campagnola, S., Strange, N. J., and Russell, R. P., "A fast tour design method using non-tangent v-infinity leveraging transfer," *Celestial Mechanics and Dynamical Astronomy*, Vol. 108, No. 2, Oct. 2010, pp. 165–186.

[41] Takubo, Y., Landau, D., and Anderson, B., "Automated Tour Design in the Saturnian System," *2023 Spaceflight Mechanics Meeting, Austin, TX, USA*, January 15-19 2023.

[42] Landau, D., "Efficient Maneuver Placement for Automated Trajectory Design," *Journal of Guidance, Control, and Dynamics*, Vol. 41, No. 7, July 2018, pp. 1531–1541.

[43] Englander, J. A., Conway, B. A., and Williams, T., "Automated Mission Planning via Evolutionary Algorithms," *Journal of Guidance, Control, and Dynamics*, Vol. 35, No. 6, Nov. 2012, pp. 1878–1887.

[44] Englander, J. A. and Conway, B. A., "Automated Solution of the Low-Thrust Interplanetary Trajectory Problem," *Journal of Guidance, Control, and Dynamics*, Vol. 40, No. 1, Jan. 2017, pp. 15–27.

[45] Conway, B. A., "A Survey of Methods Available for the Numerical Optimization of Continuous Dynamic Systems," *Journal of Optimization Theory and Applications*, Vol. 152, No. 2, Feb. 2012, pp. 271–306.

[46] Olds, A. D., Kluever, C. A., and Cupples, M. L., "Interplanetary mission design using differential evolution," *Journal of Spacecraft and Rockets*, Vol. 44, No. 5, 2007, pp. 1060–1070.

[47] Abdelkhalik, O. and Mortari, D., "N-Impulse Orbit Transfer Using Genetic Algorithms," *Journal of Spacecraft and Rockets*, Vol. 44, No. 2, March 2007, pp. 456–460.

[48] Luo, Y.-Z., Tang, G.-J., Lei, Y.-J., and Li, H.-Y., "Optimization of Multiple-Impulse, Multiple-Revolution, Rendezvous- Phasing Maneuvers," *Journal of Guidance, Control, and Dynamics*, Vol. 30, No. 4, July 2007, pp. 946–952.

[49] Luo, Y.-Z., Zhang, J., Li, H.-y., and Tang, G.-J., "Interactive optimization approach for optimal impulsive rendezvous using primer vector and evolutionary algorithms," *Acta Astronautica*, Vol. 67, No. 3-4, Aug. 2010, pp. 396–405.

[50] Rosa Sentinella, M. and Casalino, L., "Cooperative evolutionary algorithm for space trajectory optimization," *Celestial Mechanics and Dynamical Astronomy*, Vol. 105, 2009, pp. 211–227.

[51] Zhu, Z., Gan, Q., Yang, X., and Gao, Y., "Solving fuel-optimal low-thrust orbital transfers with bang-bang control using a novel continuation technique," *Acta Astronautica*, Vol. 137, Aug. 2017, pp. 98–113.

[52] Taheri, E., Arya, V., and Junkins, J. L., "Acceleration-based indirect method for continuous and impulsive trajectory design," *31st AAS/AIAA Space Flight Mechanics Meeting, AAS 21-399*, February 1-3 2021.

[53] Saloglu, K. and Taheri, E., "Acceleration-based switching surfaces for impulsive trajectory design in restricted three-body dynamics," *2022 AAS/AIAA Astrodynamics Specialist Conference, AAS 22-838, Charlotte, NC, USA, August 7-11*, 2022.

[54] Arya, V., Şaloğlu, K., Taheri, E., and Junkins, J. L., "Generation of Multiple-Revolution Many-Impulse Optimal Spacecraft Maneuvers," *Journal of Spacecraft and Rockets*, 2023, pp. 1–13.

[55] Saloglu, K., Taheri, E., and Landau, D., "Existence of Infinitely Many Optimal Equal-Delta-v Trajectories in Two-Body Dynamics," *2023 Spaceflight Mechanics Meeting, AAS 23-307, Austin, TX, USA*, January 15-19 2023.

[56] Saloglu, K., Taheri, E., and Landau, D., "Existence of Infinitely Many Optimal Iso-Impulse Trajectories in Two-Body Dynamics," *Journal of Guidance, Control, and Dynamics*, Vol. 0, No. 0, 2023, pp. 1–18.

[57] Vallado, D. A., *Fundamentals of astrodynamics and applications*, Vol. 12, Springer Science & Business Media, 2001.

[58] Russell, R. P., "On the solution to every Lambert problem," *Celestial Mechanics and Dynamical Astronomy*, Vol. 131, No. 11, Nov. 2019, pp. 50.

[59] Gooding, R. H., "A procedure for the solution of Lambert's orbital boundary-value problem," *Celestial Mechanics and Dynamical Astronomy*, Vol. 48, No. 2, 1990, pp. 145–165.

[60] Ochoa, S. I. and Prussing, J. E., "Multiple revolution solutions to Lambert's problem," *Spaceflight mechanics 1992*, 1992, pp. 1205–1216.

[61] Izzo, D., "Revisiting Lambert's problem," *Celestial Mechanics and Dynamical Astronomy*, Vol. 121, No. 1, Jan. 2015, pp. 1–15.

[62] Arora, N., Russell, R. P., Strange, N., and Ottesen, D., "Partial derivatives of the solution to the Lambert boundary value problem," *Journal of Guidance, Control, and Dynamics*, Vol. 38, No. 9, 2015, pp. 1563–1572.

[63] Battin, R. H., "Lambert's problem revisited," *AIAA Journal*, Vol. 15, No. 5, 1977, pp. 707–713.

[64] Taheri, E., Kolmanovsky, I., and Atkins, E., "Enhanced smoothing technique for indirect optimization of minimum-fuel low-thrust trajectories," *Journal of Guidance, Control, and Dynamics*, Vol. 39, No. 11, 2016, pp. 2500–2511.

[65] Perkins, F. M., "Flight mechanics of low-thrust spacecraft," *Journal of the Aerospace Sciences*, Vol. 26, No. 5, 1959, pp. 291–297.

[66] Walker, M. J., Ireland, B., and Owens, J., "A set modified equinoctial orbit elements," *Celestial mechanics*, Vol. 36, No. 4, 1985, pp. 409–419.

[67] Junkins, J. L. and Taheri, E., "Exploration of Alternative State Vector Choices for Low-Thrust Trajectory Optimization," *Journal of Guidance, Control, and Dynamics*, Vol. 42, No. 1, Jan. 2019, pp. 47–64.

[68] Mall, K. and Taheri, E., "Unified trigonometrization method for solving optimal control problems in atmospheric flight mechanics," *AIAA Scitech 2020 Forum*, 2020, p. 0022.

[69] Taheri, E. and Junkins, J. L., "Generic smoothing for optimal bang-off-bang spacecraft maneuvers," *Journal of Guidance, Control, and Dynamics*, Vol. 41, No. 11, 2018, pp. 2470–2475.

[70] Glandorf, D. R., "Lagrange multipliers and the state transition matrix for coasting arcs." *AIAA Journal*, Vol. 7, No. 2, Feb. 1969, pp. 363–365.

[71] Prussing, J. E., "A Class of Optimal Two-Impulse Rendezvous Using Multiple-Revolution Lambert Solutions," *The Journal of the Astronautical Sciences*, Vol. 48, No. 2-3, June 2000, pp. 131–148.

[72] Curtis, H., *Orbital mechanics for engineering students*, 3rd edition, Butterworth-Heinemann, 2013.